Università
Ca'Foscari
Venezia

Department of Molecular Science and Nanosystems

Master's degree

In Science and Technology of Bio-Nanomaterials

Master degree thesis

Two dimensional nanoplateletes for water splitting

Supervisors

Prof. Alberto Vomiero

Prof. Elisa Moretti

Co-supervisor

Dr. Kamran Akbar

Graduant

Laura Dal Compare

862672

Academic year

2020/2021

Acknowledgements

During the writing of this thesis I received a great deal of support.

First of all, I would like to thank my supervisors, Professors Alberto Vomiero and Elisa Moretti, for their guide and support since the very first exams of this master's degree. Their lessons inspired me to where I am now and without them this work would have never been accomplished. I would like to thank also Professor Isabella Concina, my supervisor at LTU, for hosting me in a new university and making me feel part of the research group. Thank You for all the kind suggestions.

Thank You Dr. Kamran Akbar and Getachew Solomon for the patient support and for teaching me new techniques and skills for carrying out this research work.

I would like to thank also my colleagues which accompanied me during this master's degree and this internship at LTU. In particular, thank you Edlind Lushaj: your support during these years and, in particular in this internship, was a valuable help, especially in the darkest moments.

I must thank also my family, especially my parents and Ilaria, for the wise suggestions and sympathetic ear. You are always there for me.

Abstract

The subject of this research work is the synthesis and characterization of 2 dimensional, 2D, materials, namely graphitic carbon nitride (g-C_3N_4) and layered double hydroxides, LDHs, for applications in energy conversion. g-C_3N_4 system was synthesized through a simple pyrolysis method with different precursors (thiourea and urea) and temperatures (400, 440, 500, 550, 600 °C). The exfoliation of the as-synthesized photocatalyst into 2D nanosheets was performed using an ultrasonic treatment to enhance the photocatalytic activity. NiCo-LDH (NiCo layered double hydroxide) system was also obtained using a co-precipitation method at 90 °C. To further enhance the catalytic performance of the as-synthesized 2D systems, single metal atoms were anchored on 2D sheet structure. In particular, selected metals (Ni, Co, Cu in the case of g-C_3N_4 and Ru and Pt for NiCo LDH) were deposited on the synthesized 2D materials with a loading of 0.5 wt%. The crystalline structure of the as-synthesized 2D systems was investigated with X-ray diffraction (XRD), while their morphology and composition were studied through field emission-scanning electron microscopy (FE-SEM) and energy-dispersive spectroscopy (EDS). g-C_3N_4-based samples underwent diffuse reflectance UV-vis spectroscopy to investigate their optical properties. The structure of LDH samples was further assessed through Raman spectroscopy. Finally, the samples were tested for electrochemical and photoelectrochemical water splitting to investigate their catalytic applicability.

Index

1. Introduction

1.1 Two-dimensional nanomaterials

Given the increasing global energy consumption and therefore the need for developing routes for sustainable energy conversion and storage, the investigation of materials with unique characteristics able to promote energy efficiency is a topic of primary focus. For this purpose, 2 dimensional (2D) nanomaterials have attracted a lot of attention since the discovery of graphene. In fact, this kind of material shows unique chemical, physical, optical and electronic properties, including high specific surface area, ultrathin structure, optimal electron transmission capability and high anisotropy. Furthermore, it is possible to modify their properties while maintaining their structural stability through atomic engineering thanks to a large fraction of surface atoms. Among the possible strategies, it is necessary to mention elemental doping, creation of pores, vacancy, strain, edge, phase engineering and construction of 2D heterostructures. This may enable to optimize the surface electronic state, reduce the reaction energy barrier and therefore improve their intrinsic activity [1].

There are many examples of studied 2D materials, including transition metal dichalcogenides (TMDs), graphitic carbon nitride (g-C_3N_4), layered double hydroxides (LDHs), layered double oxides, hexagonal boron nitride (*h*-BN), black phosphorus (BP), Mxenes, Xenes, perovskites, metal-organic frameworks (MOFs) and covalent-organic frameworks (COFs) [1-3].

These materials can be further distinguished between layered and non-layered materials, according to differences in chemical bonding, crystal phases and composition. Non-layered structures mainly include 2D metals, metal chalcogenides, polymers, and organic-inorganic hybrid perovskites, and their properties are generally affected by the composition and the crystal phases: different crystal phases can be obtained by regulating the arrangement of atoms and the stacking mode of the layers. Instead, graphene, *h*-BN, *g*-C3N4, BP, TMDs, LDHs, 2D MOFs, and layered metal oxides are examples of layered

structures. Each layer of a 2D layered material consists of few or single-atom-thick covalently bond lattice. These materials, therefore, lack dangling bonds and since the chemical bonds on the surface are fully saturated, the neighbouring layers experience Van der Waals interactions. This allows to exfoliate them into ultrathin 2D nanosheets [1].

1.2 Graphitic carbon nitride (g-C_3N_4)

Graphitic carbon nitride has a general formula of $(C_3N_3H)_n$ and it is a polyconjugated semiconductor composed of carbon and nitrogen atoms with a layered graphite-like structure (**figure 1.2.1**) [4].

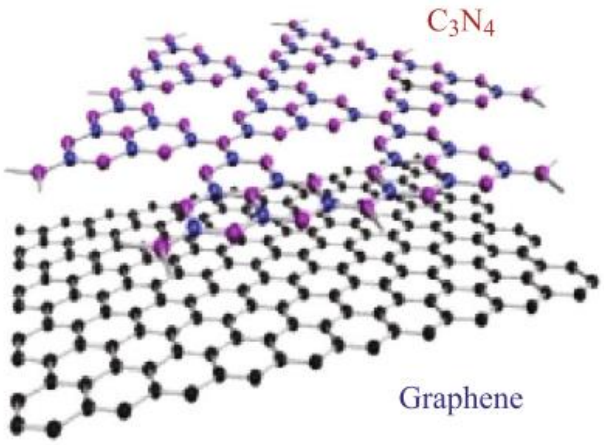

Figure 1.2.1. Schematic of the 3D g-C_3N_4/graphene structure: comparison between layers of graphene and g-C_3N_4, constituted by tri-s-triazine units.

It is one of the oldest polymers reported in the literature since it was first synthesized by Berzelius and named "melon" by Liebig in 1834. g-C_3N_4 is regarded as the most stable allotrope of covalent carbon nitride solids at ambient conditions [3-5].

Analogous to graphite, graphitic carbon nitride is organized in stacked layers, with covalent C-N bonds, which are held together by Van der Waals forces. In each layer tri-s-triazine units as shown in **figure 1.2.2.** are connected with planar amino groups, thus forming a structure that provides the polymer thermal (600 °C in the air) and chemical stability in both acidic and alkaline environments [5].

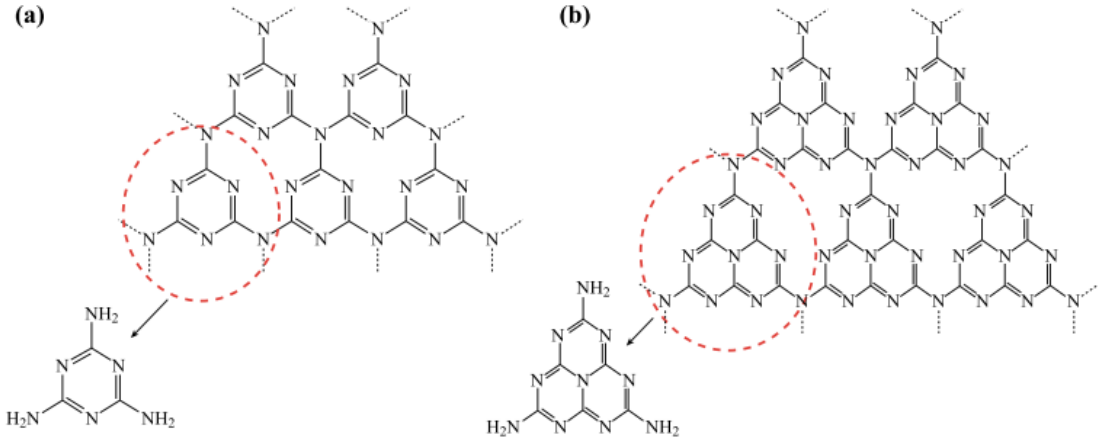

Figure 1.2.2. (a) Triazine and (b) tri-s-triazine (heptazine) structures of g-C_3N_4 [5].

In addition to the high thermal and chemical stability, g-C_3N_4 displays other interesting physicochemical properties including photoelectrochemical properties, inoxidizability, biological compatibility and waterproofness. Furthermore, it is non-toxic, metal-free, made of earth-abundant elements and therefore economic and environmentally friendly. These qualities make it a promising candidate for photocatalysis-driven applications and in the degradation of organic pollutants, hydrogen evolution from water, sensing, imaging, and energy conversion. Further, g-C_3N_4 is a semiconductor with a band gap energy of about 2.7 eV, therefore active in the visible region and thus an ideal candidate to harvest abundant sunlight [3-5].

Various morphologies of g-C_3N_4 including mesoporous, bulk, and different structures like 3D, 2D, 1D, and 0D materials can be obtained [6-8]. The structure of g-C_3N_4 can be controlled by a variety of synthetic routes, including different condensation temperatures, different ratios of precursors, porosity induced by hard/soft templating strategies, and exfoliation and doping [9]. Since the focus of this work of research is mainly on 2D materials as support for the cited applications, the other materials (3D, 1D, 0D) and the corresponding synthetic routes will not be discussed further.

1.2.1. Bulk g-C_3N_4

Bulk g-C_3N_4 can be synthesized from a variety of nitrogen-rich organic precursors. In particular, the most used ones are melamine, cyanamide, urea and thiourea. Thermal decomposition of g-C_3N_4 precursors has become the most used procedure since it is cost-effective and easy to perform [5,10]. For instance, many reports presented the efficient synthesis of g-C_3N_4 by heating urea without additional assistance. The condensation of g-C_3N_4 is facilitated by oxygen compounds which act as additional leaving motifs, thus allowing structural perfection. The possible reaction mechanism for the conversion of urea into a g-C_3N_4 network at high temperatures is reported in **figure 1.3.3** (top) [5, 11, 12].

Thiourea is a common and low-cost raw material, with a similar molecular structure to urea, but with easy-leaving groups of sulfur species. It can form g-C_3N_4 networks by condensation at high temperatures as shown in **figure 1.3.3.** (bottom). The as-synthesized g-C_3N_4 showed increased visible light absorbance, promoted charge separation and a high visible light photocatalytic activity compared to other precursors such as dicyandiamide and even urea [12,13].

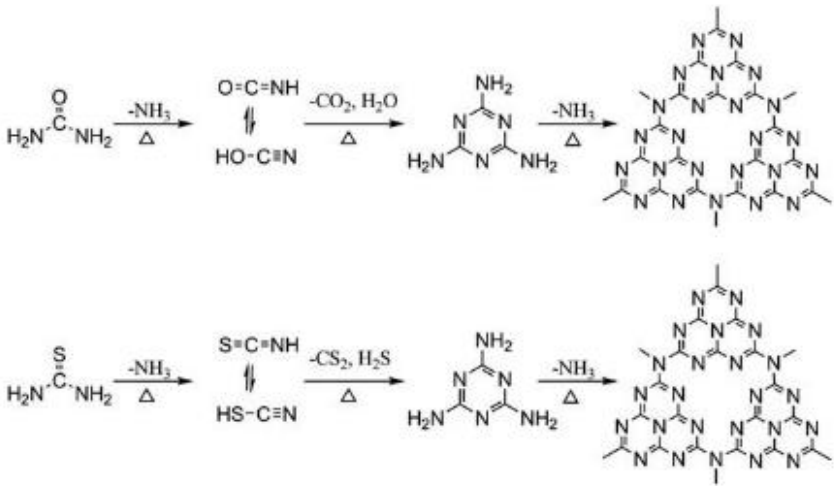

Figure 1.3.3. Reaction mechanisms describing the self-polymerization of urea (top) and thiourea (bottom) into a g-C_3N_4 network at high temperatures [12].

Both precursors are usually heated in a range of temperatures between 400 and 650 °C, with a particular focus at 500-600 °C. In particular, graphitic-like networks are formed but are usually incomplete at 450 °C, while the formation of the typical graphitic-like layered structure can be observed at 500 °C. Further increasing the temperature to 550 and 600 °C can optimize the polycondensation of g-C_3N_4, but excessive thermal energy, for instance at 650 °C, can compact the structure to such an extent that it can induce the decomposition of the g-C_3N_4 polymer [11].

Nevertheless, the synthesized bulk g-C_3N_4 has weak photocatalytic effectiveness due to several factors including low specific surface area and fast recombination rate of the photo-generated electrons and hole pairs, the particle boundary effects which interrupt the delocalization of electrons, low effectiveness for electron and hole separation, wide band gap, poor electronic conductivity and inadequate visible light absorption since g-C_3N_4 can absorb only blue light of the solar spectrum which limits the usage of the whole solar spectrum [14].

Several strategies have been investigated to improve the photocatalytic performance and meet the industrial demand for stability and efficiency. Examples of them are doping of metals and non-metal elements, construction of heterojunctions, sensitizing with organic dyes and controlling morphology [9, 11,14]. Among them, the reduction to nanosheets has been demonstrated to be an impactful strategy since it significantly affects the electronic and optical properties of the material, thus improving the photocatalytic activity.

1.2.2. g-C_3N_4 nanosheets

Ultrathin 2D nanosheets have attracted extensive attention since they exhibit incredible electronic, optical, and biocompatible properties if compared to bulk materials. The exfoliation of carbon nitrides into ultrathin nanosheets may enhance the photocatalytic activity due to the surface and quantum confinement effect, via the exposure of active sites and optimized light-harvesting, charge separation and percolation [5, 15-19].

The two main approaches to synthesize 2D g-C_3N_4 nanosheets are the top-down approach, which consists of the exfoliation of layered g-C_3N_4 solids into free-standing nanosheets (e.g. post-thermal oxidation etching process [16,17] and ultrasonication-assisted liquid exfoliation route), and the bottom-up approach, in which the g-C_3N_4 nanosheets can be obtained from the anisotropic assembly of organic molecules in a 2D manner (**Figure 1.3.4**) [18].

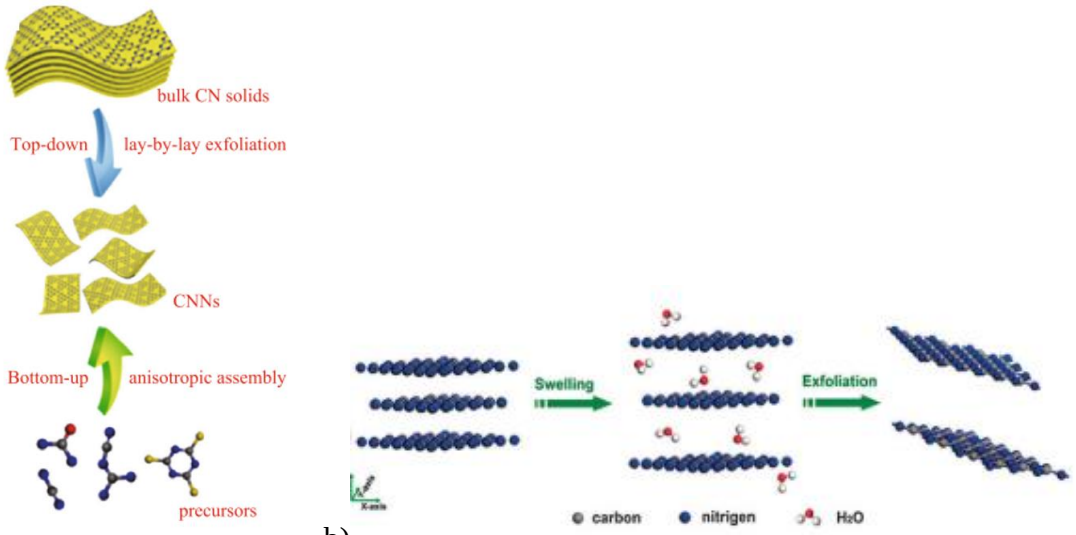

a) b)

Figure 1.3.4. Schematic illustration of top-down and bottom-up synthetic strategies for g-C_3N_4 nanosheets (a) and of the liquid exfoliation process from bulk to ultrathin nanosheets (b) [18].

In particular, continuous ultrasonication of bulk g-C_3N_4 in solvents allows the preparation of nanosheets as well (**figure 1.3.4b**). Different solvents can be used to suspend bulk g-C_3N_4, such as IPA, N-methyl-pyrrolidone (NMP), water, ethanol, and acetone. The as-synthesized dispersions are then sonicated at room temperature for the gradual exfoliation into nanosheets with the increase of sonication time. After sonication, the dispersion is centrifuged to remove the aggregates, thus obtaining a homogenous dispersion of g-C_3N_4 nanosheets. However, the g-C_3N_4 nanosheets obtained in solvents may suffer from some defects such as the introduction of impurity and undesired functional groups, which could therefore prevent their further applications [19,20].

1.3 Layered double hydroxides (LDHs)

LDHs have recently attracted considerable research interest due to their high electrocatalytic activity, earth abundance, ultrastability, and low-toxicity. They are a class of lamellar solids also known as hydrotalcites or anionic clays. Most LDHs have a similar structure as mineral hydrotalcite (HT), $[Mg_6Al_2(OH)_{16}](CO_3)\cdot 4(H_2O)$, which was the first LDH discovered. Mineral hydrotalcite is a natural magnesium–aluminium hydroxyl carbonate whose name derives from its water content (hydro) and also because of its resemblance to talc (talcite) [21,22].

These compounds have layered crystal structures (shown in **figure 1.3.1**) generally consisting of layers with octahedrally coordinated divalent metal cations replaced by trivalent ones, thus forming positively charged host layers. Exchangeable inorganic or organic anions are located in the interlayers compensating for the positive charge. Furthermore, hydrogen bonds link the hydroxyl groups of the host layers to the anions or water molecules. The general formula of LDH is $[M^{2+}_{1-x}\, M^{3+}_{x}(OH)_2\,](A^{n-}\,)_{x/n}\cdot mH_2O$, where M^{2+} and M^{3+} are divalent and trivalent metal cations, respectively, and A^{n-} is an interlayer n-valent anion [21-27].

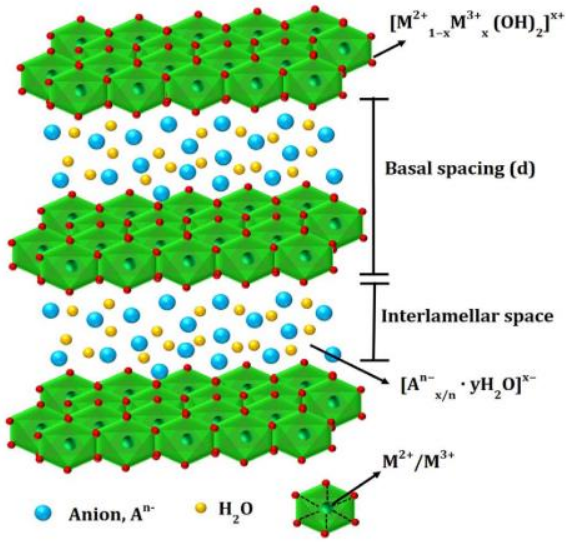

Figure 1.3.1. Schematic of the structure of layered double hydroxides [21].

By tuning many parameters, including the nature of the metal cations and exchangeable charge-compensating anions and M^{2+}/ M^{3+} molar ratios, wide variations in the structure and therefore in the material are possible, obtaining a large number of host-guest assemblies and nanoarchitectures that may play a role in the design of desirable physical and chemical properties. They possess high active surface area, confinement effect, and abundant base active sites, useful for catalytic reactions [25,26].

Since this kind of material could be suitable for many different applications, ranging from electrocatalysis, photoelectrocatalysis, adsorption materials to additives in polymers, etc., these properties have been tailored to fulfill each of them in the best way. For instance, both M^{2+} and M^{3+} are involved in redox reactions during the OER (Oxygen Evolution Reaction) catalytic process (shown in **figure 1.3.2**) by adsorbing and desorbing reactants, intermediates, and products. Therefore, electron transfer may occur between the divalent and trivalent cations M^{2+} and M^{3+} in the process, while A^{n-}, which compensate for the positive charge, thus acting as counterion, may influence the adsorption/desorption process on the surface of the LDH host layer and/or in the interlayer space [27].

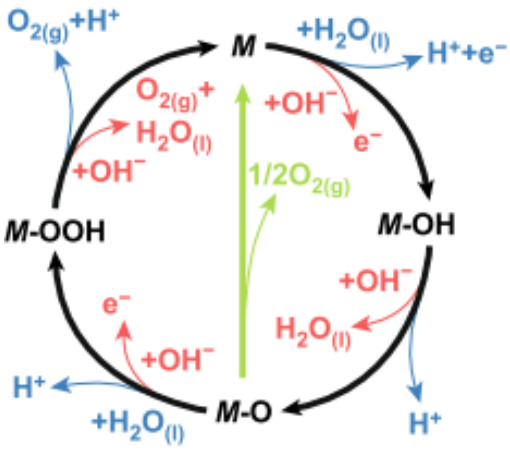

Figure 1.3.2. OER mechanisms in acid (blue) and alkaline (red) conditions for LDHs [27].

The lateral size and thickness of LDHs play an important role in chemical and physical properties. In particular, the reduction of the thickness to a nanometre or molecular scale, thus resulting in the formation of nanosheets, can further increase the number of exposed active sites and the specific surface area. As a result, the intrinsic electrocatalytic activity

of the material is improved, the transport of reactant species is made easier and consequently the activity toward water splitting is promoted [27-29].

LDH can be synthesized via various routes. Among them, widely used synthetic methodologies are the co-precipitation route (direct method), ion-exchange route (indirect method), and reconstruction /rehydration route (memory-effect method).

The co-precipitation method is the most frequently applied and consists of the slow addition of a solution containing the target anion to be intercalated into a solution of divalent and trivalent metal cations in an appropriate stoichiometric ratio. The pH is then increased by the addition of a base or hydrolysis of urea, leading to the precipitation of the LDH. This procedure allows the synthesis, also in large-scale, of LDH with a variety of divalent and trivalent cations and different anions, from inorganic anions, (e.g. Cl^{-}, NO^{3-}, and CO_3^{2-}) to organic molecules and even large biomolecules.

In the anion-exchange route, LDH is first prepared by co-precipitation method and then the LDH precursor is stirred in a solution containing an excess of anion to replace the ones already present in the interlayer region, preferably in an inert atmosphere to avoid carbonate intercalation. This exchange process mainly relies on the electrostatic forces between the exchanging anions and the positively charged layers.

Rehydration of LDH consists first in calcination at temperatures of about 400–500 °C, thus transferring the materials to the respective metal oxides and consequently removing interlayer water molecules, hydroxyl groups of LDH and intercalated anions. Finally, LDH is regenerated back by immersing these mixed metal oxides in water or any other solution of anions. Many different anions have been successfully incorporated in LDH with this method, which is also very useful for the intercalation of organic molecules [21].

1.4 Single-atom catalysis

Single-atom catalysts refer to supported metal catalysts where metals are monodispersed as single atoms on the surface of given supports like carbon materials, metal oxides and metal hydroxides. This can lead to great advantages compared to supported metal

nanoparticles catalyst, where only the outer surface of the particle takes part in the catalytic cycles since it is accessible to reagents, while the portion of metals in the inner part is wasted. Therefore, reduction of the nanoparticles to small clusters of atoms and eventually single atoms increases the ratio of surface metal atoms exposed and consequently the number of approachable atoms, as shown in **figure 1.4.1**. Hence, the size of the metal particles is one of the factors that affect the performance of the catalyst more significantly [30-33].

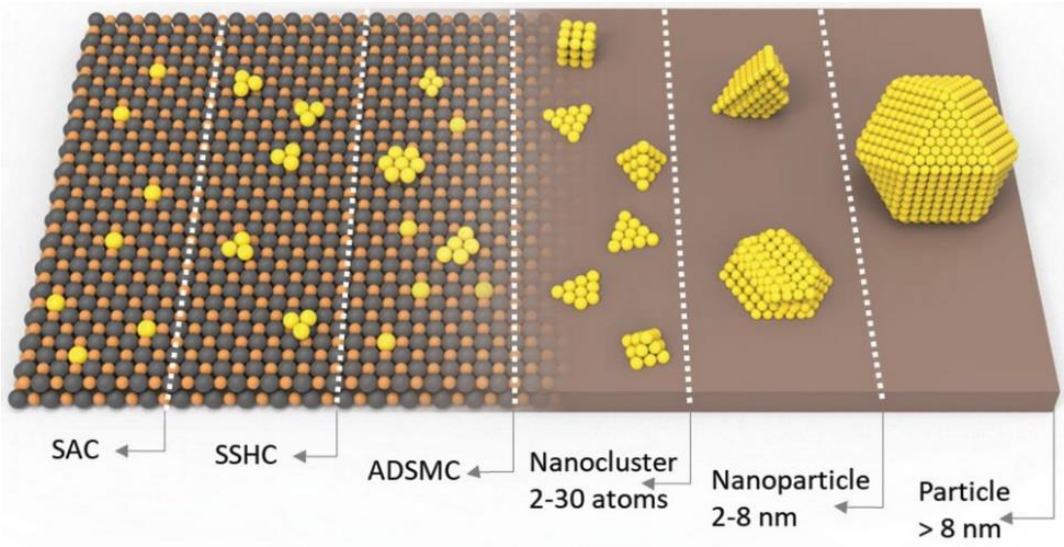

Figure 1.4.1. Schematic illustration of SAC, SSHC (single site heterogeneous catalysts), ADSMC (atomically dispersed supported metal catalyst), nanocluster of metal atoms, nanoparticles and metal particles [34].

As a result, each of the metal atoms on the surface of the support may act as a catalytic center, thus allowing to maximize the atomic efficiency of the metals. The anchored metal atoms are thought to directly interact with the support via charge transfer. This results in two effects: the positively charging of the single atoms and the partial activation of the metal atoms constituting the support. This metal atom-support interaction strongly affects the catalytic performance and explains why different metal atoms anchored on the same support or same metal atoms on different supports exhibit different activities [30, 35].

Another great difference compared to nanoparticles is the relationship between stability and reactivity. The adsorption behaviour of supported metal nanoparticles is related to

their density of states and this plays an important role in defining their catalytic behaviour. While the nanoparticles' atoms anchoring on the surface of the support may not be the actual active sites, the anchoring sites and the active sites coincide in a single atom catalyst, as anticipated. The balance between activity and stability is a key factor to take into account: metal atoms with the highest stability might not be the most active ones. However, a solid knowledge on the dynamic nature of the supported single metal atoms during a targeted catalytic reaction is still lacking [35].

SACs were also studied to increase the selectivity of the conventional catalyst supports. Structural irregularities are present on the surface of clusters of metal atoms and nanoparticles, therefore where the catalysis occurs is unclear. Since surface reactivity and surface free energy are related, atoms with the same chemical composition but different positions on the surface of the support have different surface reactivity. However, this different surface reactivity eventually leads to a worsened selectivity toward the desired reaction in a system of competing reactions [33]. To nanoparticles or clusters of atoms, single atoms only have one site for adsorption and therefore their active sites are intrinsically better defined, as expected. This catalytic behaviour indeed recalls that of homogeneous catalysts. However, the presence of the support structure in the proximity to the single atoms increases the heterogeneity of SACs' active sites, making the ideal uniform activity of homogeneous catalysts impossible to achieve. Nevertheless, appropriate choice of the support structure, like 2D materials can make single atoms more accessible to reagents, thus improving the catalytic performance and uniform activity. Consequently, single-atom catalysts can be regarded as a bridge between homogeneous and heterogeneous catalysts and high selectivity can be achieved under appropriate conditions [30, 35, 36].

The first challenge that we can meet in the preparation of single-atom catalysts is the tendency to aggregate the metal atoms at high loadings like 1% or higher, which unfortunately would be ideal for industrial production. Secondly, commonly tested support material does not possess uniform surfaces, as a result the single atoms are experiencing different chemical environments at different sites. Hence, a support with high surface area which can establish strong interactions with metal atoms is preferred to obtain SACs with high performances [30, 37]. In this regard, 2D materials are an interesting choice to overcome these challenges. As mentioned before, 2D materials are

good platforms thanks to their large surface area and abundant sites for anchoring metal atoms. This allows to achieve higher loadings (> 0.5 wt%) than the ones commonly obtained for 3D materials (below 0.5 wt%). Furthermore, metal atoms on 2D materials have higher chances to interact with the reactants than 3D supports since they are less coordinatively saturated and can be approached by the reactants from either sides of the supports layer [30].

1.5 Applications of g-C_3N_4 and LDH systems

As mentioned in paragraph 1.1, 2D nanomaterials have attracted growing interest in research on many energy-related processes, including electrocatalysis, photocatalysis, solar cells, batteries and supercapacitors, thanks to their unique electronic and structural properties. Among them, applications such as electrocatalysis and photoelectrocatalysis are particularly interesting, owing to their ability to produce various renewable fuels in a sustainable way [38]. Shifting from fossil-fuels towards renewable sources appears to be key in this process. One of the methods allowing the production of energy through this route is the splitting of water into hydrogen and oxygen, according to equation 1. The optimum energy density/mass ratio of hydrogen (120–142 MJ/kg) make it a promising clean fuel [39–43].

$2H_2O \rightarrow O_2 + 2H_2$ (1)

Electrochemical water splitting (WS). It occurs in an electrolysis cell made up of anode, cathode and an aqueous electrolyte (**figure 1.5.1**) thanks to two half-reactions, hydrogen evolution reaction (HER, eq. 2, **figure 1.5.1b**), which occurs at the cathode, and oxygen evolution reaction (OER, eq. 3, **figure 1.5.1b**), at the anode [44,45] [39–48].

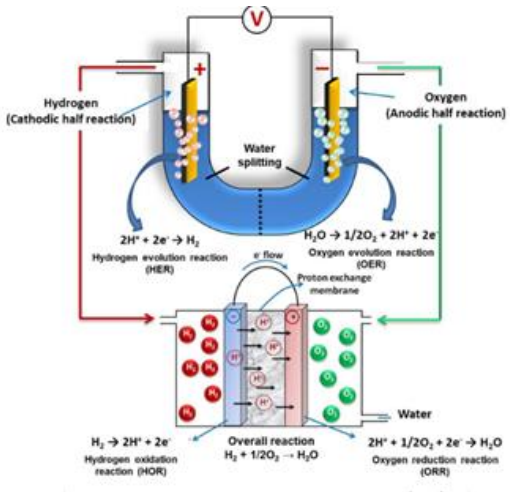

a)

b)

Acidic HER: $4e^- + 4H^+ \rightarrow 2H_2$ (2a)

Basic HER: $4H_2O + 4e^- \rightarrow 2H_2 + 4OH^-$ (2b)

Acidic OER: $2H_2O \rightarrow O_2 + 4e^- + 4H^+$ (3a)

Basic OER: $4OH^- \rightarrow O_2 + 2H_2O + 4e^-$ (3b)

Figure 1.5.1. a) Schematic representation of oxygen reduction reaction (ORR) in a fuel cell, oxygen evolution reaction (OER), and hydrogen evolution reaction (HER) by water hydrolysis and b) HER and OER half-reactions occurring in acidic and basic media [48].

An excess potential called overpotential which is higher than the theoretical thermodynamic potential (1.23 V at 25° and 1 atm) must be applied to carry out the WS process [41,47]. Its practical use is therefore limited and overpotential must be decreased for the process to be efficient [48-50]. Furthermore, to attain large current densities suitable for industrial applications, hydrogen evolution and oxygen evolution catalysts should be highly active and display long-term stability [46,48].

Photoelectrochemical (PEC) WS. It was first discovered by Fujishima and Honda [51] In 1972 and is regarded as one of the most promising approaches to convert solar energy into clean hydrogen fuels [52–54]. As electrochemical WS, the PEC cell is usually composed of a photoanode and a cathode in an aqueous environment [55]. Furthermore, a light source and a semiconductor material are needed for the conversion of photons (with energies greater or equal to the energy band gap (Eg)) into chemical energy [56,57]. The electrons are excited towards the conduction band (CB) and generate holes that remain in the valence band (VB) [53]. Water oxidation occurs if the VB potential is more positive than the O_2/H_2O redox potential, while water reduction occurs when the CB is more negative than H^+/H_2 redox potential [53,58]. Highly efficient solar-chemical energy conversion strongly depends on the design of novel photoelectrodes with the addition of the following critical points: (i) photogenerated electron (e-) and hole (h+) pairs must reach the catalyst surface rapidly and the diffusion lengths should be large to avoid their

fast recombination; (ii) photoelectrode specific surface area should be large to enhance the adsorption of water molecules; (iii) surface reactions kinetics should be high [59]. Moreover, the best semiconductor for PEC WS should have a bandgap lower than 3.0 eV to gain a wide range of solar light absorption, but larger than 1.23 eV to have proper band-edge potentials for water-splitting reaction and excellent stability in photochemical reactions [60].

1.6 Aim of the thesis

The aim of this research work is the synthesis of 2D materials, in particular graphitic carbon nitride (g-C_3N_4) and layered double hydroxides (LDH), thanks to the unique properties described in the previous paragraphs. Furthermore, the 2D nature of g-C_3N_4 opens the possibility to use it also for single-atom catalysis: the combination of the high catalytic activity of single-atom metal sites with the photo-response characters of g-C_3N_4 promises great potential in the field of photocatalysis. As for the single metal atoms to be dispersed, in the case of g-C_3N_4, particular attention has been given to selected non-noble and low-cost metals (Co, Ni and Cu), to investigate if it is possible to obtain performance comparable or even higher than those obtained employing the more studied but also more expensive noble metals. Also, LDH are believed to be alternative supports for precious metal catalysts, since their base active sites can also provide special anchoring sites for the supported noble metal atoms like Au, Pt, Ru. In this way the single metal atoms may be inserted/anchored orderly on LDHs, thus inheriting the atomic dispersion feature of the LDH structure. Consequently, selected precious metals (Pt and Ru) are deposited on LDH. The synthesized materials are then tested for electrochemical (LDH) and photoelectrochemical (g-C_3N_4) water splitting, to investigate their catalytic performances and verify if they are suitable for the theorized applications.

2. Methods

This chapter discusses the synthesis of the bare 2D materials and their hybrids with anchored single metal atoms on their surfaces. We focused on the synthesis of graphitic carbon nitride and NiCo layered double hydroxide, thanks to their promising properties discussed in paragraphs 1.3 and 1.4. First, the synthesis of the bare materials is presented, then how single-atom catalysis was successively performed on them is discussed.

2.1 List of reactants

The list of reactants employed for the synthesis described in the following paragraphs is reported in **Table 2.1**.

Table 2.1. List of the reactants employed for the syntheses.

Reactant	**Formula**	**Molecular weight (g/mol)**	**Purity**	**Purchased from**
Thiourea	CH_4N_2S	76.12	99.00 %	Sigma Aldrich
Urea	CH_4N_2O	60.06	99.00 %	Sigma Aldrich
Nickel(II) nitrate hexahydrate	$Ni(NO_3)_2 \cdot 6H_2O$	290.81	98.50 %	Sigma Aldrich
Cobalt(II)nitrate hexahydrate	$Co(NO_3)_2 \cdot 6H_2O$	291.03	98.00 %	Sigma Aldrich
Ruthenium(III) chloride trihydrate	$RuCl_3 \cdot 3H_2O$	261.43	99.95 %	Sigma Aldrich
Hexachloroplatinic acid	H_2PtCl_6	409.81	> 99.00 %	Sigma Aldrich
Nickel(II) acetate tetrahydrate	$Ni(OCOCH_3)_2 \cdot 4H_2O$	248.84	98.00 %	Sigma Aldrich
Copper chloride(II) dihydrate	$CuCl_2 \cdot 2H_2O$	170.48	99.99 %	Sigma Aldrich
Cobalt(II) chloride hexahydrate	$Cl_2Co \cdot 6H_2O$	237.93	98.00 %	Sigma Aldrich
Sodium borohydride	$NaBH_4$	37.83	98.00 %	Sigma Aldrich

Ethylene glycol	$C_2H_6O_2$	62.07	99.00 %	Sigma Aldrich
Ethanol	C_2H_5OH	46.07	99.8 %	Sigma Aldrich
2-Propanol	C_3H_8O	60.1	> 99.5 %	Sigma Aldrich
Deionized water	H_2O	18.02		

2.2 Synthesis and exfoliation of graphitic carbon nitride (g-C_3N_4)

Graphitic carbon nitride was prepared through a simple direct pyrolysis method (as reported in paragraph 1.2.1) which leads to the thermal decomposition of the chosen precursors and consequently to a self-polymerization of the CN network. Among the many possibilities (melamine, dicyandiamide, and so on), thiourea and urea were chosen as precursors owing to their cost-effectiveness [12]. In most of the reports these precursors are heated directly at 500 or 550 °C in air. Instead, in this work of research an optimized ramp-up method by first heating the precursors (5 g) to 400 °C for three hours was investigated and developed. This was done to induce a first self-polymerization of the precursors, thus stabilizing the powder after the initial decomposition steps. Then, thiourea was further heated to 440, 500, 550 and 600 °C, while samples of graphitic carbon nitride from urea were obtained by heating at 440, 500 and 550 °C. In both cases a ramp of 5 °C/min was applied. The as-synthesized samples are reported in **tables 2.2** and **2.3**.

Table 2.2. Samples of g-C_3N_4 prepared by using thiourea as the precursor, together with their different calcination temperatures.

Sample	**Precursor**	**$T_{c,1}$ (°C)** **First calcination temperature**	**$T_{c,2}$ (°C)** **Second calcination temperature**
T_g-C_3N_4_400	NH_2CSNH_2	400	/
T_g-C_3N_4_440	NH_2CSNH_2	400	440
T_g-C_3N_4_500	NH_2CSNH_2	400	500
T_g-C_3N_4_550	NH_2CSNH_2	400	550
T_g-C_3N_4_600	NH_2CSNH_2	400	600

Table 2.3. Samples of g-C_3N_4 prepared by using urea as the precursor, together with their different calcination temperatures.

Sample	Precursor	$T_{c,1}$ (°C) First calcination temperature	$T_{c,2}$ (°C) Second calcination temperature
U_g-C_3N_4_440	NH_2CONH_2	400	440
U_g-C_3N_4_500	NH_2CONH_2	400	500
U_g-C_3N_4_550	NH_2CONH_2	400	550
U_g-C_3N_4_600	NH_2CONH_2	400	600

After calcination, a yellow powder with some brownish spots on the wall was obtained for thiourea, while a white/very pale-yellow powder resulted from the thermal decomposition of urea (**figure 2.2.1**). In both cases, a reduction in the final amount was observed, as expected from the mechanism of the reaction. These results are coherent with the ones reported by literature [12,13]. The resulting powders were ground in a mortar.

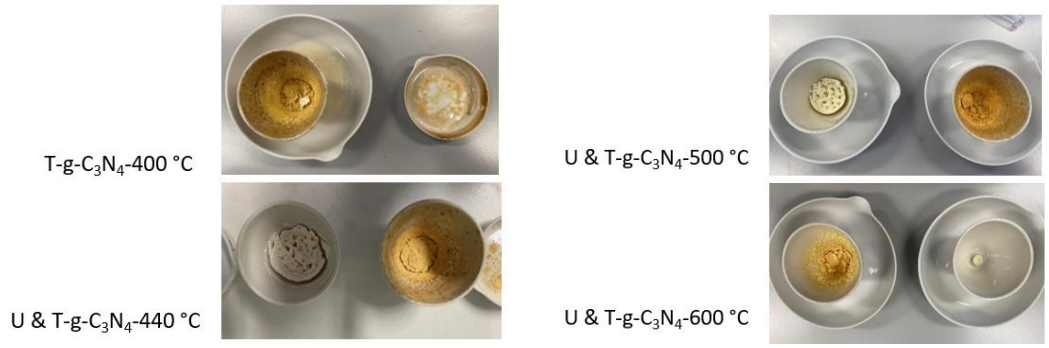

Figure 2.2.1. Pictures of T_g-C_3N_4_400, T_g-C_3N_4_440, T_g-C_3N_4_500, T_g-C_3N_4_600, U_g-C_3N_4_440, U_g-C_3N_4_500 and U_g-C_3N_4_600 after calcination.

To proceed with the successive step of depositing atoms from metal salts on the surface of the support, the same process was scaled up by calcinating 30 g of thiourea with the same ramp and reaching a temperature of 550 °C. The same precursor and temperature were chosen among the other samples by taking into account the amounts obtained in the previous steps and the outcomes of the characterization analyses (XRD, UV-Vis and band

gap energy) performed on the samples, as reported in **tables 2.2** and **2.3** in paragraph 3.1.3.

The as-synthesized carbon nitride (from now on labelled as B-g-C_3N_4, bulk graphitic carbon nitride) successively underwent a process of mechanical exfoliation (one pulse every other second for three/four hours), to obtain the desired 2D nanosheets from the bulk material. A solution of g-C_3N_4 in isopropyl alcohol (IPA) was prepared and sonicated using an Ultrasound XL 2020 [19]. The resulting solution was centrifuged first at 3000 rpm for 2 minutes to separate the phases and remove the aggregates, and then at 9000 rpm for 10 minutes to collect the exfoliated product. The resulting powders were dried in an oven (65 °C) overnight and eventually ground in a mortar. This sample of exfoliated carbon nitride was labelled as E- g-C_3N_4 and is shown in **figure 2.2.2**.

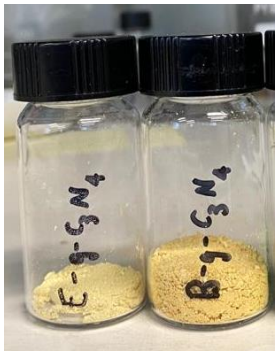

Figure 2.2.2. Pictures of E-g-C_3N_4 (left) and B-g-C_3N_4 (right) powders.

2.3 Single-atom catalysis on g-C_3N_4

Single atoms were deposited on the previously synthesized 2D support by a wet chemical method [61,62]. 200 mg of B-g-C_3N_4 were first dispersed in H_2O (100.0 mL) under sonication for 1h. Then, the desired metal precursor, among $Ni(OCOCH_3)_2 \cdot 4H_2O$, $Cl_2Co \cdot 6H_2O$ and $CuCl_2 \cdot 2H_2O$ (0.5 wt% metal relative to the support) was added and the slurry was stirred in the dark at room temperature for 1 h. Next, $NaBH_4$ was added dropwise and stirred overnight to achieve the reduction of the metal. Finally, the solids

were separated by centrifugation and washed three times with H_2O and ethanol. The resulting powders were dried in an oven (65 °C) overnight and eventually ground in a mortar. The as-synthesized samples were labelled as Ni/g-C_3N_4, Co/g-C_3N_4 and Cu/g-C_3N_4 and are reported in **table 2.4** and shown in **figure 2.3.1**.

Table 2.4. Samples of g-C_3N_4 with single metal atoms (Ni, Co and Cu) deposited on them, together with their carbon nitride precursor (thiourea) and single metal atom precursors.

Sample	Carbon nitride precursor	Single metal atom precursor
Ni/g-C_3N_4	NH_2CSNH_2 (550 °C)	$Ni(OCOCH_3)_2 \cdot 4H_2O$
Co/g-C_3N_4		$Cl_2Co \cdot 6H_2O$
Cu/g-C_3N_4		$CuCl_2 \cdot 2H_2O$

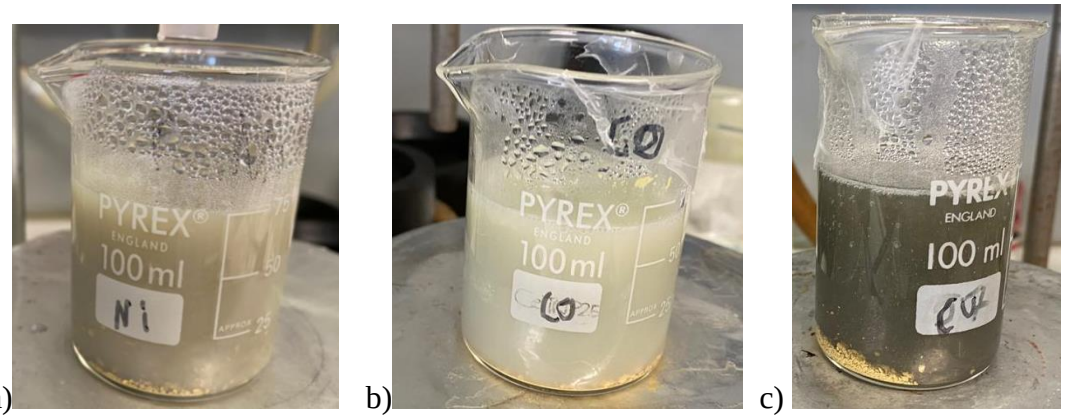

Figure 2.3.1. Pictures of Ni/g-C_3N_4 (a), Co/g-C_3N_4 (b) and Cu/g-C_3N_4 (c) after the addition of the reducing agent $NaBH_4$.

2.4 Synthesis of layered double hydroxides

NiCo LDH was prepared by first dissolving $Ni(NO_3)_2 \cdot 6H_2O$ and $Co(NO_3)_2 \cdot 6H_2O$ with molar ratios Ni:Co 1:1.26 and 1:2 in a mixture solvent of 15.0 mL deionized water and 37.5 mL ethylene glycol inside a round-bottom flask. Then, 37.5 mmol of urea was added under stirring: hydrolyzation of urea leads to the production of ammonia, thus creating

the basic environment necessary for the development of the layered structure. The resulting solution was then refluxed under vigorous magnetic stirring for 3 h at 90 °C [63]. Finally, the precipitates were centrifuged and washed three times with deionized water. The resulting products were both a green and light powder, as shown in **figure 2.4.1.**

Figure 2.4.1. Pictures of NiCo LDH after 3 hours of reflux (left) and after drying (right).

2.5 Single-atom catalysis on NiCo LDH

Pt/NiCo LDH_1:1.26 and 1:2 were prepared by first dissolving $Ni(NO_3)_2 \cdot 6H_2O$ and $Co(NO_3)_2 \cdot 6H_2O$ with molar ratios Ni:Co 1:1.26 and 1:2, respectively, together with H_2PtCl_6 (to obtain a metal loading of 0.5 wt%) in a mixture solvent of 15.0 mL deionized water and 37.5 mL ethylene glycol inside a round-bottom flask. Then, urea was added under stirring and the resulting solution was then refluxed under vigorous magnetic stirring for 3 h at 90 °C, as before. Finally, the precipitates were centrifuged and washed three times with distilled water.

Ru/NiCo LDH_1:1.26 and 1:2 were synthesized similarly by adding $RuCl_3 \cdot 3H_2O$ (0.5 wt%) to the mixture of nickel and cobalt nitrates, deionized water and ethylene glycol and repeating the same steps as before.

The as-synthesized samples are reported in **table 2.5**.

Table 2.5. Samples of NiCo LDH without and with single metal atoms (Pt and Ru) deposited on them, together with the support precursors and molar ratios and the single metal atom precursors.

Sample	Precursors	Ni:Co molar ratio	Single metal atom precursor
NiCo_1:1.26	$Ni(NO_3)_2{\cdot}6H_2O$ $Co(NO_3)_2 \cdot 6H_2O$	1:1.26	-
Ru/NiCo_1:1.26		1:1.26	$RuCl_3 \cdot 3H_2O$
Pt/NiCo_1:1.26		1:1.26	H_2PtCl_6
NiCo_1:2		1:2	-
Ru/NiCo_1:2		1:2	$RuCl_3 \cdot 3H_2O$
Pt/NiCo_1:2		1:2	H_2PtCl_6

2.6 Characterization techniques

The as-synthesised samples were characterized with different techniques and instruments at the Department of Engineering Sciences and Mathematics at Luleå University of Technology, LTU. The crystal structures of the as-synthesized samples were studied with powder X-ray diffraction (XRD). XRD patterns of the samples were acquired by using a PANalytical Empyrean X-ray diffraction diffractometer, 2θ ranging from 5 to 80°, and utilizing Cu Kα source. The reference patterns were provided by P analytical High Score software. Field emission-scanning electron microscopy (FE-SEM) equipped with energy-dispersive spectrometry (EDS) was performed to study their surface morphology and elemental distribution. SEM images were taken with Magellan XHR 400L Field Emission Scanning Electron Microscope with a 5 kV electron beam, while EDS analysis was carried out using EDAX Energy-dispersive X-ray Spectroscopy. To perform analysis, g-C_3N_4 samples were dispersed in ethanol and coated on FTO glass. The optical properties of g-C_3N_4 samples were probed with diffuse reflectance UV-vis spectroscopy using a Agilent Cary 5000 UV-vis spectrophotometer in the range 200-800 nm. Raman spectroscopy on LDH samples was carried out on Raman Spectrometry (Senterra Raman

spectrometer from Bruker equipment, using a 532 nm laser source for excitation) in the ambient environment.

2.7 Electrochemical measurements

LDH samples underwent OER measurements in a common three-electrode configuration at room temperature using ModuLab XM ECS potentiostat (Solartron instrument). An Ag/AgCl electrode and a modified glassy carbon electrode (GCE) were used as a reference and counter electrodes, respectively. The working electrode consisted of a GCE (3 mm diameter) with a small amount of the catalyst deposited on it. The catalyst was prepared by adding 5 mg of the sample to 600 μl of isopropanol and 20 μl of Nafion. All electrochemical measurements were performed in alkaline media (1M KOH, pH=14) and the potential was converted to a reversible hydrogen electrode (RHE) through Nerst equation $E\ (vs\ RHE) = E(vs\ Ag/AgCl) + 0.059 * pH + 0.1976\ V$. Linear sweep voltammetry (LSV) was conducted with a scan rate of 10 mV/s in a potential window from 1.02 to 2.02 V (vs RHE). Cyclic voltammetry (CV) was repeated at different scan rates (20, 40, 60, 80, 100, 120, 140, 160, 180, 200 mV/s) in a potential window from 1.07 to 1.27 V (vs RHE). Electrochemical impedance spectroscopy (EIS) was measured at 1.62 V (vs RHE) over the frequency spectrum range from 100 kHz to 0.03 Hz at an amplitude of 10 mV.

2.8 Photoelectrochemical measurements

Photoelectrochemical measurements were carried out in a three-electrode configuration at room temperature using ModuLab XM ECS potentiostat (Solartron instrument) under light and no light conditions. An Ag/AgCl electrode and Pt foil were used as a reference and counter electrodes, respectively. The photoanodes were prepared in the following way. First, FTO glasses were cleaned with distilled water, isopropanol and ethanol using an ultrasonicator. Then, 50 mg of powder, 1.0 mL of α-terpineol and an appropriate amount of a gel made of cellulose and ethanol (3 g in 40.0 mL) were mixed creating a

homogeneous paste, which was then deposited on FTO glass by Doctor Blading technique. The as-prepared photoanodes were finally heated at 200 °C on the hot plate. All photoelectrochemical measurements were performed in 0.1M $NaSO_4$ (pH=7) and the potential was converted to a reversible hydrogen electrode (RHE) through Nerst equation $E\ (vs\ RHE) = E(vs\ Ag/AgCl) + 0.059 * pH + 0.1976\ V.$ Linear sweep voltammetry (LSV) was conducted with a scan rate of 5 mV/s in a potential window from 0.41 to 1.81 V (vs RHE). The transient photocurrent response was measured at a voltage of 1.01 V (vs RHE). Electrochemical impedance spectroscopy (EIS) was measured at 1.21 V (vs RHE) over the frequency spectrum range from 100 kHz to 0.03 Hz at an amplitude of 10 mV.

3. Results and discussion

This chapter discusses the results of characterizations and tests performed on the samples synthesised as described in Chapter 2. In particular, the outcomes of the characterizations ad tests of g-C_3N_4 and LDH samples are reported separately.

3.1 g-C_3N_4 samples

This section discusses the results of structural, morphological and optical characterizations (X-ray diffraction, scanning electron microscopy, energy-dispersive spectrometry and UV-Vis spectroscopy) and photoelectrochemical water splitting performed on the g-C_3N_4 samples.

3.1.1 XRD analysis

The diffraction patterns of the g-C_3N_4 samples prepared from thiourea (T-g-C_3N_4) and urea (U-g-C_3N_4) at different temperatures have been analysed to verify their crystalline structure. Furthermore, E-g-C_3N_4, Ni/g-C_3N_4, Co/g-C_3N_4 and Cu/g-C_3N_4 were also analysed to investigate if changes in the crystalline structure occurred during the synthetic procedures. They are reported together with the reference patterns in the following figure (**figure 3.1.1.1**).

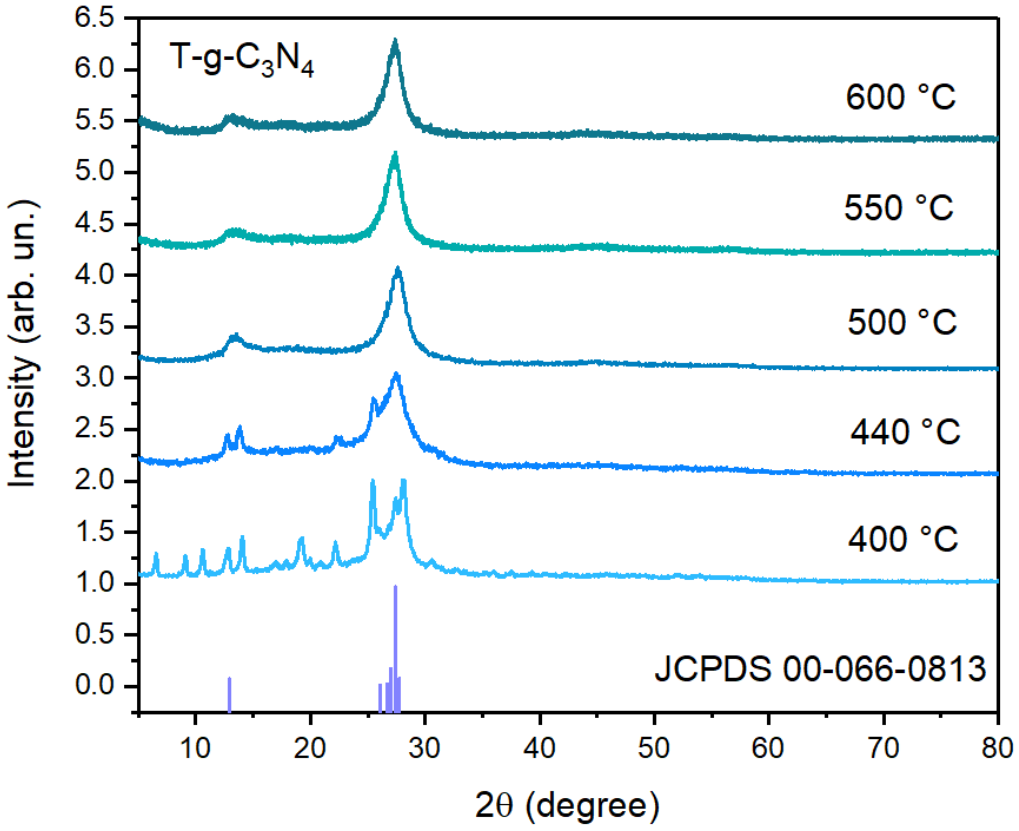
T-g-C3N4
600 °C
550 °C
500 °C
440 °C
400 °C
JCPDS 00-066-0813
Intensity (arb. un.)
2θ (degree)

a)

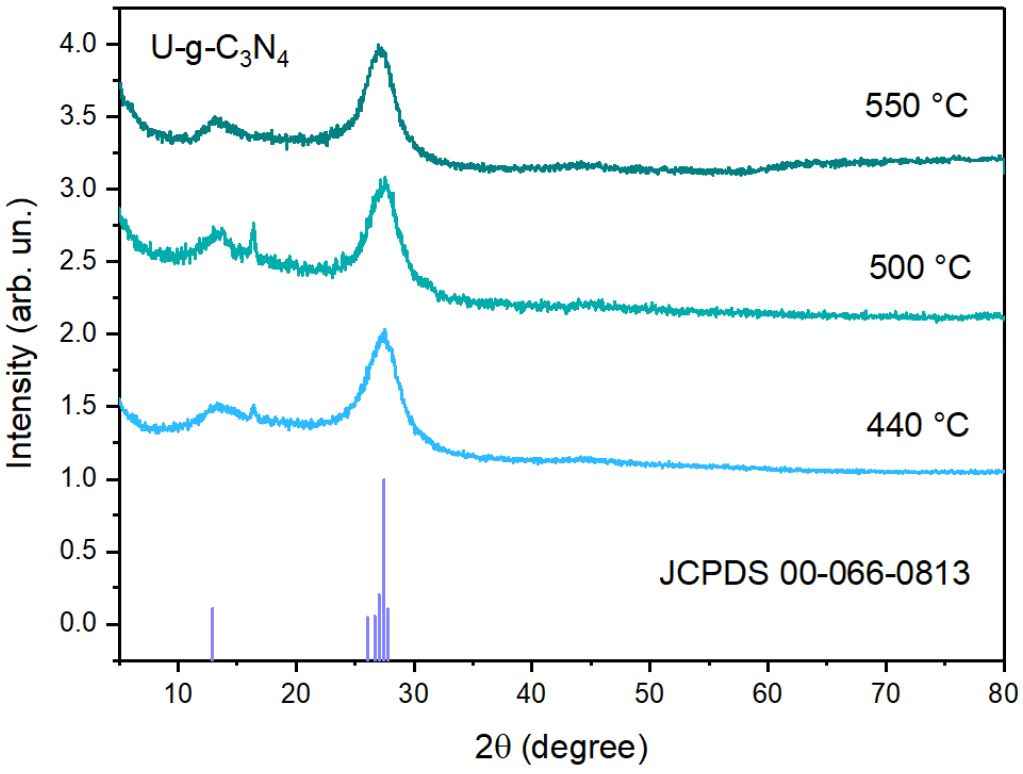
U-g-C3N4
550 °C
500 °C
440 °C
JCPDS 00-066-0813
Intensity (arb. un.)
2θ (degree)

b)

Figure 3.1.1.1. XRD patterns of g-C_3N_4 samples prepared from thiourea (T-g-C_3N_4, a) and urea (U-g-C_3N_4, b) at different temperatures: in the case of T-g-C_3N_4, 600, 550, 500, 440 and 400°C (from the top to the bottom) and 550, 500 and 440 °C for U-g-C_3N_4 (from the top to the bottom). The experimental patterns are compared with the reference data provided by the software (JCPDS 00-066-0813).

In the XRD patterns of the samples synthesized from thiourea and urea, two main peaks are observed. The intense peak at ~27.3° of 2θ is due to the interplanar stacking of aromatic systems and corresponds to the plane (002) of carbon nitride and a smaller one at ~13.1° can be assigned to an in-planar structural stacking motif corresponding to the plane (100) [15]. Further, the comparison of the experimental XRD data with the reference one provided by the software (JCPDS 00-066-0813) confirms that the crystalline structure of the synthesized samples is one of graphitic carbon nitride C_3N_4 as expected. Moreover, it is an orthorhombic system, with space group P21212 and space group number 12. The position of the peaks is almost the same at the different temperatures indicated in **figure 3.1.1.1**: 27.5° and 13.4° of 2θ for T-g-C_3N_4-400, 440 and 500 °C and U-g-C_3N_4-440 and 500 °C, while T-g-C_3N_4-550 and 600 °C and U-g-C_3N_4-550 °C have peaks at 27.3° and 13.1°. In particular, in the case of T-g-C_3N_4, it is possible to appreciate the transition leading to the full formation of the CN network, and therefore of g-C_3N_4 [12]. At 400 °C, graphitic-like networks are formed but are incomplete because the reaction temperature is too low to provide enough energy for condensation to occur. This is evident by the appearance of smaller peaks in the pattern due to the presence of intermediates of reaction in the crucible. They can still be noticed at 440 °C but with lower intensity, indicating the progression in the formation of the typical graphitic-like layered structure, which can be observed when the temperature is increased to 500 °C. Further increasing the temperature to 550 and 600 °C can optimize the polycondensation of g-C_3N_4.

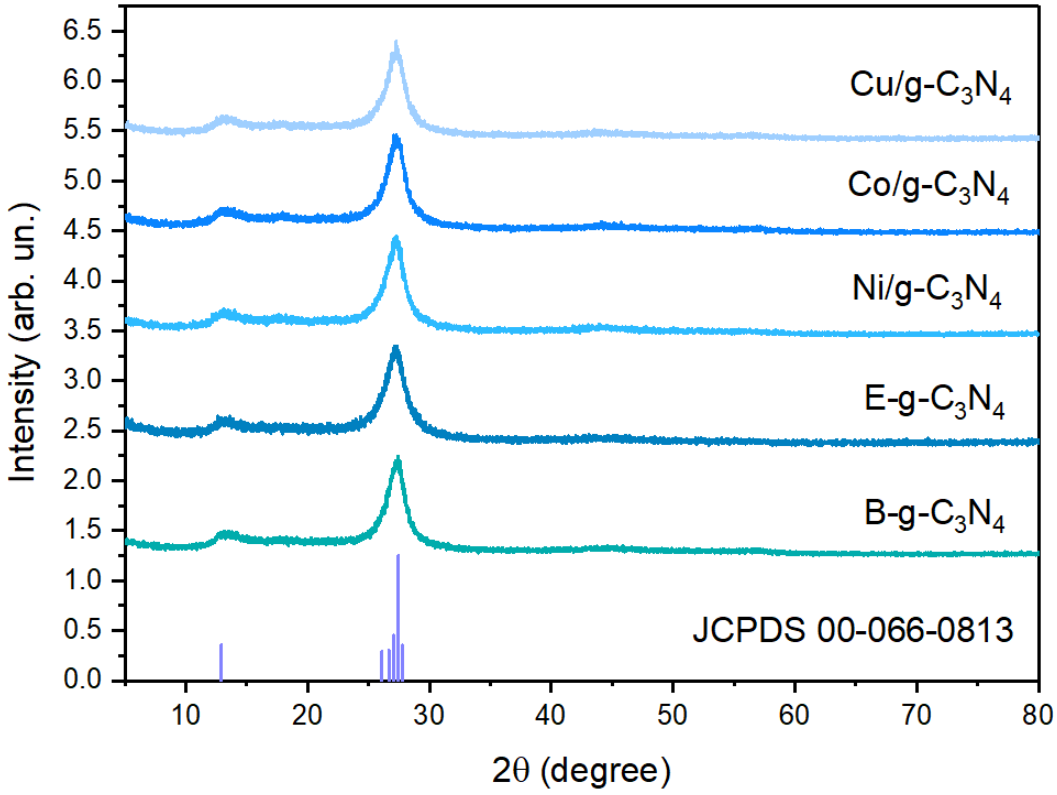

Figure 3.1.1.2. XRD patterns of B-g-C_3N_4, E-g-C_3N_4, Ni/g-C_3N_4, Co/g-C_3N_4 and Cu/g-C_3N_4 (from the bottom to the top). The experimental patterns are compared with the reference data provided by the software (JCPDS 00-066-0813).

Table 3.1.1. Table reporting the position of the peaks present in the patterns reported in **figure 3.1.1.2** together with the corresponding width.

Sample	Peak position (° of 2θ)		FWHM (full width at half maximum)
B-g-C_3N_4	13.2	27.3	2.30
E-g-C_3N_4	13.1	27.2	2.69
Ni/g-C_3N_4	13.1	27.3	2.43
Co/g-C_3N_4	13.1	27.3	2.40
Cu/g-C_3N_4	13.1	27.3	2.43

The main peaks attributed to g-C_3N_4 are present also in the XRD patters reported in **figure 3.1.1.1** with the positions indicated in **table 3.1.1** [12, 13, 15]. Furthermore, comparing the experimental data with the reference pattern provided by the software (JCPDS 00-066-0813), it is possible to conclude that the crystalline structure of E-g-C_3N_4, Ni/g-C_3N_4, Co/g-C_3N_4 and Cu/g-C_3N_4 (prepared from the bulk g-C_3N_4) is the same of B-g-C_3N_4 (the one previously known as T-g-C_3N_4-550). The phase is confirmed to be graphitic carbon nitride C_3N_4, with space group P21212 and space group number 12. No significant difference in the peak position of the different samples can be noticed, thus indicating that the interlayer distance is not modified during the synthetic procedure. No additional peaks are observed in the patterns of Ni/g-C_3N_4, Co/g-C_3N_4 and Cu/g-C_3N_4 compared to g-C_3N_4. Therefore, this technique does not allow to confirm the presence of Ni, Co and Cu, due to the very low amount of metal loading (0.5 wt%). The width at FWHM of the peaks is reported in **table 3.1.1**. Although all the samples exhibit the same bulk structure (as shown in paragraph 3.1.2), Ni/g-C_3N_4, Co/g-C_3N_4 and Cu/g-C_3N_4 show the same width, while B-g-C_3N_4 has a narrower peak. It is therefore possible to attribute this smaller width to the presence of larger grains and aggregates in B-g-C_3N_4. On the contrary, the E-g-C_3N_4 peak exhibits peak broadening compared to the other samples, probably due to a less stacked structure obtained after exfoliation.

3.1.2 SEM and EDS analysis

SEM images of B-g-C_3N_4, E-g-C_3N_4, Ni/g-C_3N_4, Co/g-C_3N_4 and Cu/g-C_3N_4 were taken to study their morphology, while their elemental composition was investigated through EDS. EDS spectra, together with the corresponding elemental mapping images, are reported in the following figures from **figure 3.1.2.1** to **3.1.2.5**. The tables in the inset provide an estimate of the ratios in atomic percentage concentration.

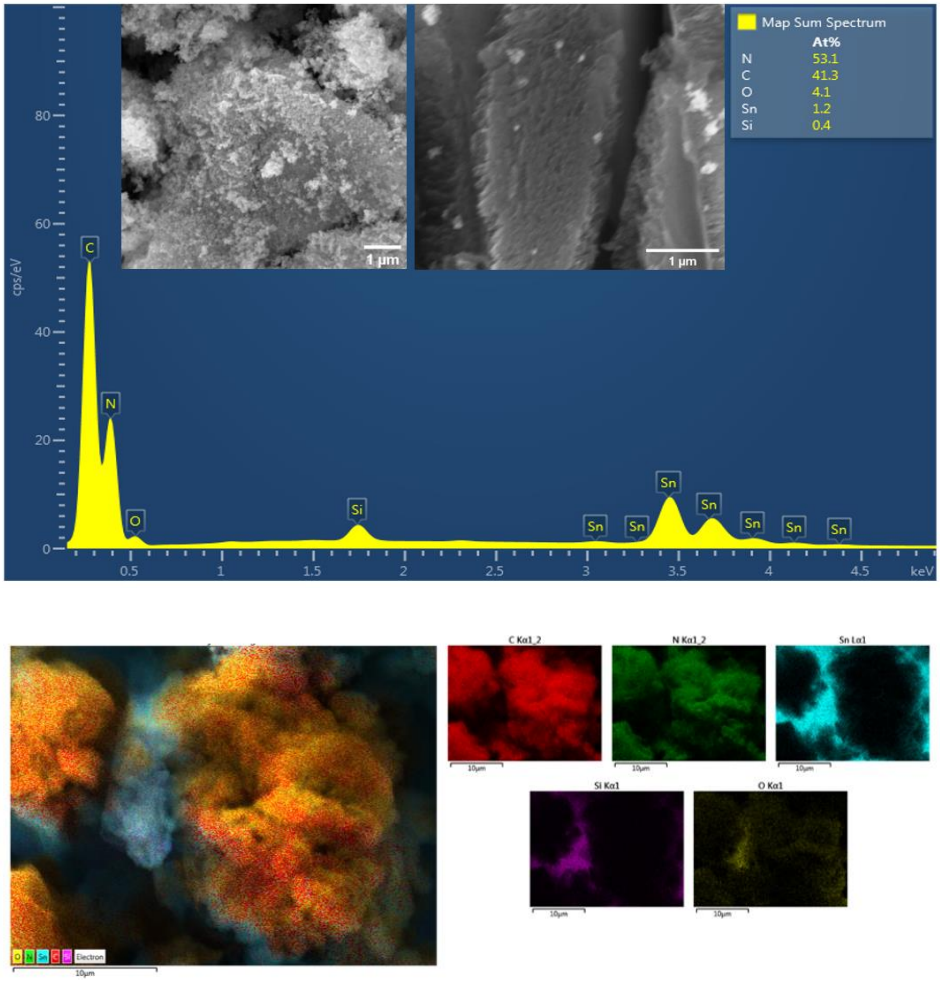

Figure 3.1.2.1. SEM images (in the inset) and EDS spectrum and elemental mapping of B-g-C_3N_4.

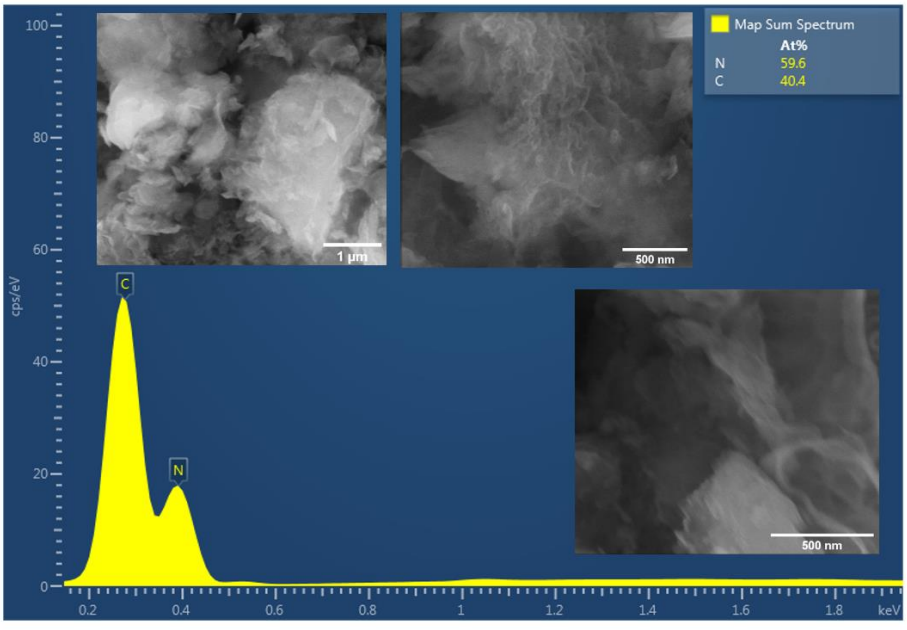

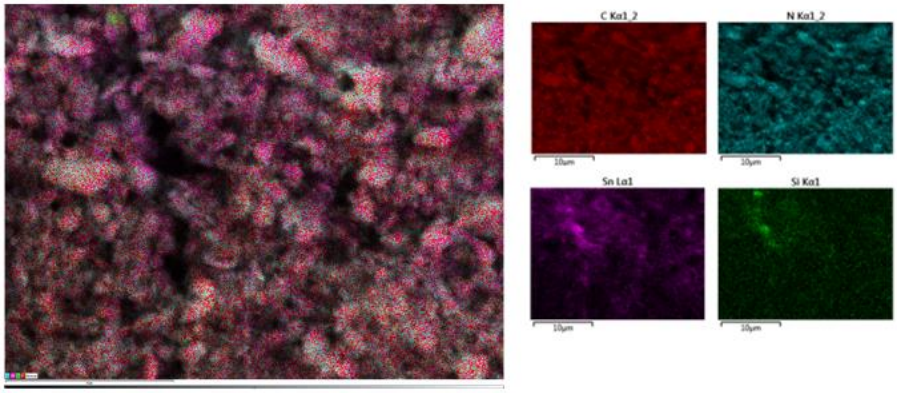

Figure 3.1.2.2. SEM images (in the inset) and EDS spectrum and elemental mapping of E-g-C_3N_4.

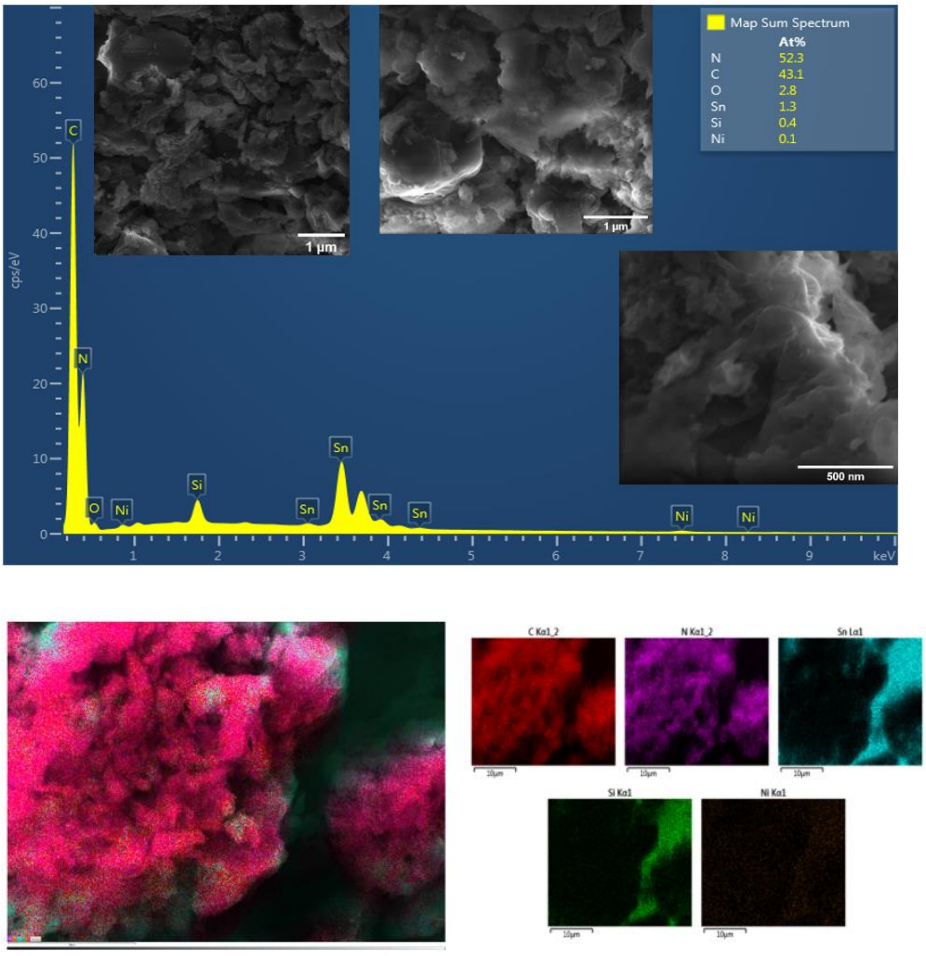

Figure 3.1.2.3. SEM images (in the inset) and EDS spectrum and elemental mapping of Ni/g-C_3N_4.

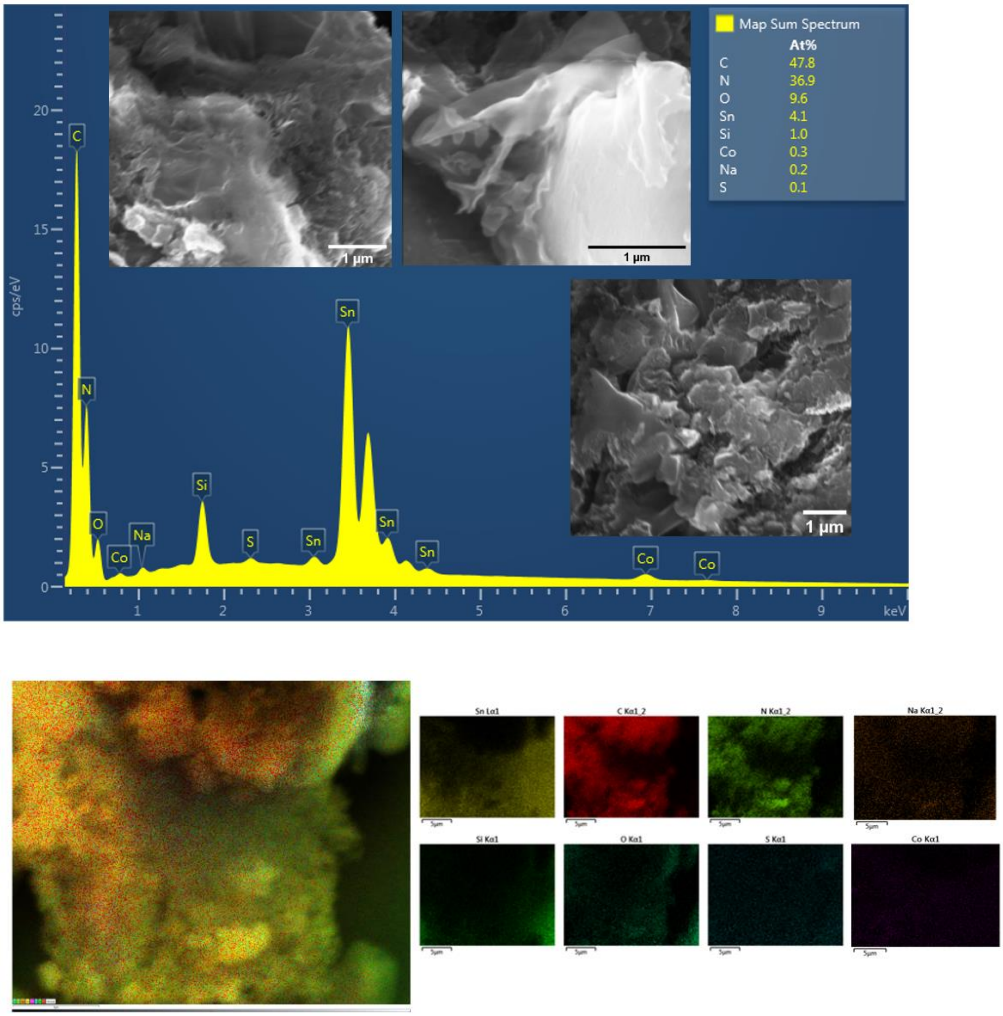

Figure 3.1.2.4. SEM images (inset) and EDS spectrum and elemental mapping of Co/g-C_3N_4.

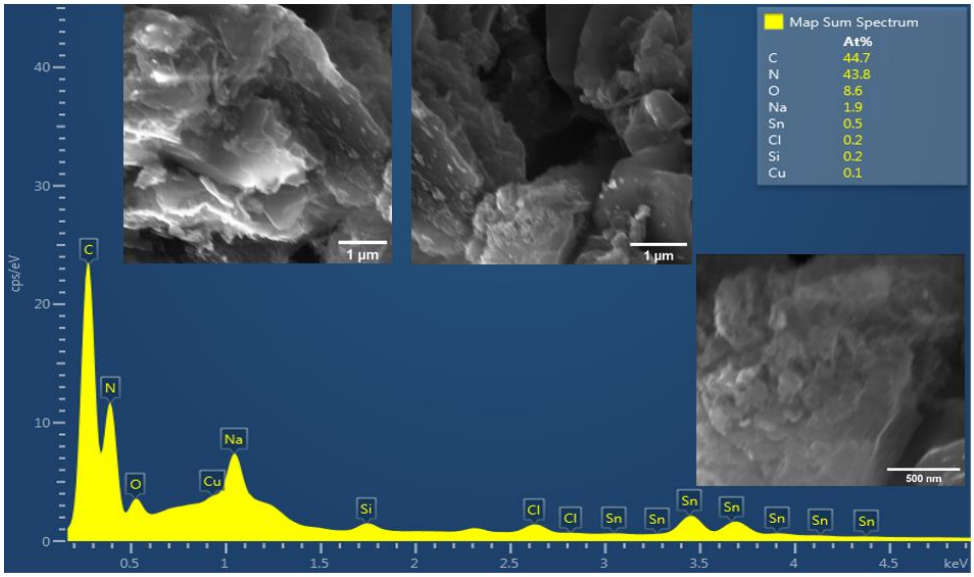

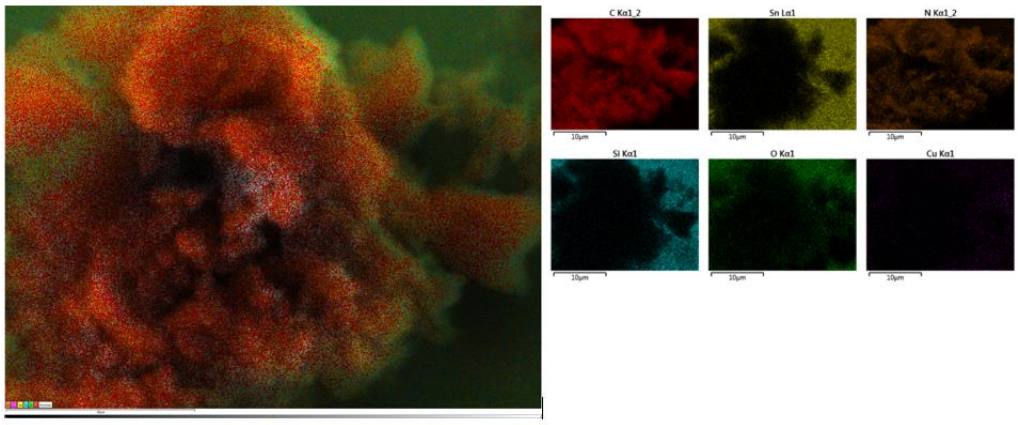

Figure 3.1.2.5. SEM images (in the inset) and EDS spectrum and elemental mapping of Cu/g-C_3N_4.

In the SEM micrographs reported above, in particular of B-g-C_3N_4, Ni/g-C_3N_4, Co/g-C_3N_4 and Cu/g-C_3N_4, it is possible to identify the bulk structure of the materials. Furthermore, structures like nanosheets can also be observed. This is particularly evident in **Figures 3.1.2.3**, **3.1.2.4**, **3.1.2.5** at high magnification (500 nm), which indicates that it is possible to separate them from the bulk structure upon exfoliation. SEM images of E-g-C_3N_4 show a less stacked structure compared to the other samples even at low magnification (1 μm), with clearly distinguishable nanosheets at high magnification, as expected. In the case of Ni/g-C_3N_4, Co/g-C_3N_4 and Cu/g-C_3N_4, it is not possible to find any proof of the presence of Ni, Co and Cu from the SEM images, not even as nanoparticles, however these elements are detected by EDS analysis and the corresponding elemental mapping. It is also possible to notice the presence of aggregates of carbon nitride in most of the samples. However, this problem could be easily solved by dispersing the samples in ethanol and sonicating.

The highest peaks in the EDS spectra of all the samples are assigned to C and N, thus confirming their presence and the formation of the CN network, as expected from the synthetic procedure. It is also possible to notice the presence of many smaller peaks of Sn and Si in most of the samples, which are due to the substrate (FTO). Furthermore, peaks of Na are present in **Figure 3.1.2.4** and **3.1.2.5** with also the presence of Cl in **figure 3.1.2.5**: they are probably leftovers from the synthesis. Furthermore, EDS analysis and elemental mapping managed to detect the presence of distributed species of Ni, Co and

Cu in Ni/g-C_3N_4, Co/g-C_3N_4 and Cu/g-C_3N_4, thus confirming the expected composition for all the synthesised samples. To verify if such elements are deposited as single atoms, other characterization techniques should be employed, including HAADF-STEM and STM. EXAFS and XANES could instead provide information on the electronic and geometrical structure of the metal species.

3.1.3 UV-Vis spectroscopy

UV-vis spectroscopy was performed on all the samples of g-C_3N_4 to investigate their optical properties. The diffuse reflectance spectra and Tauc plots, which allowed to determine the band gap values of the obtained systems, are reported below from **figure 3.1.3.1** to **3.1.3.3**.

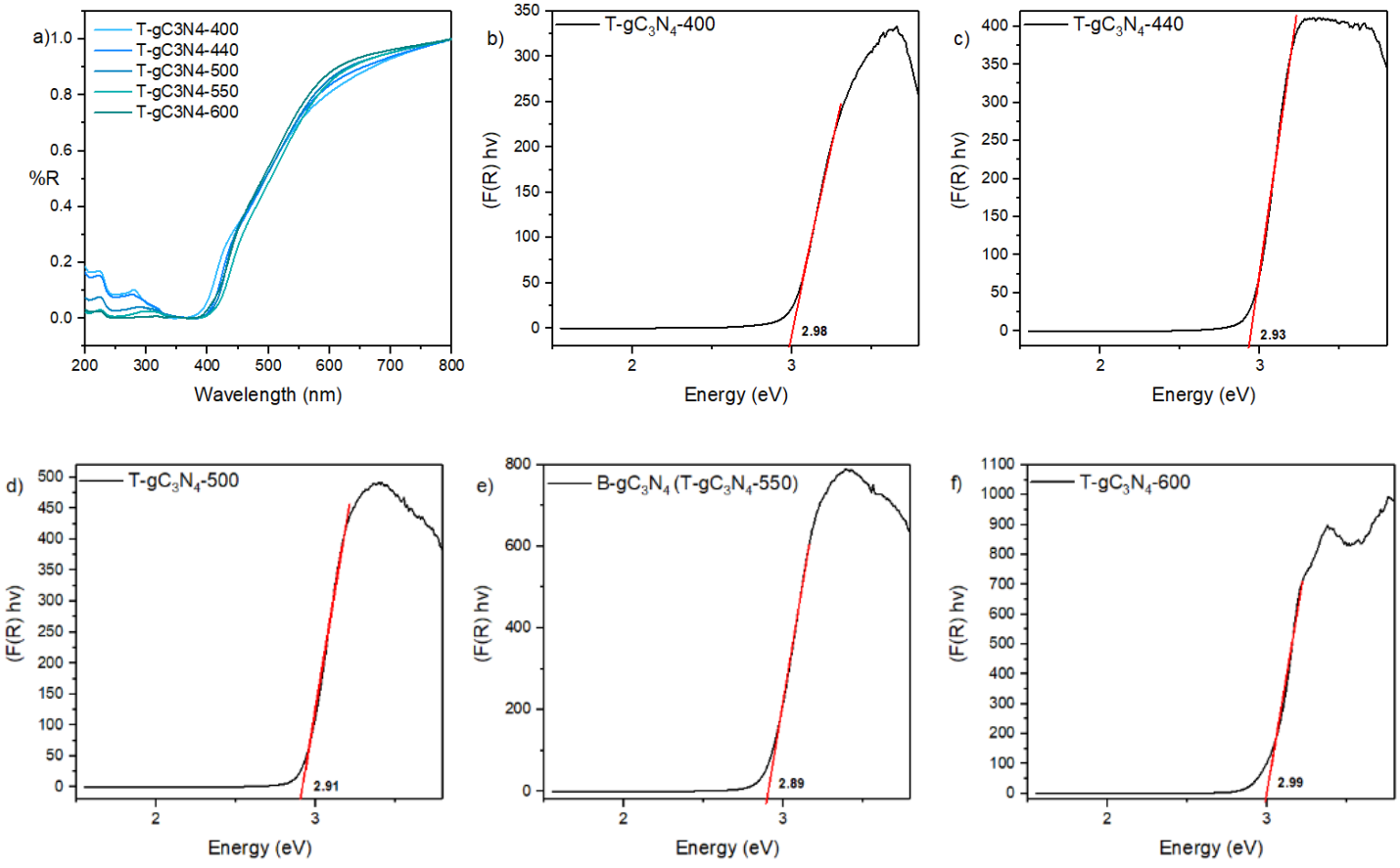

Figure 3.1.3.1. (a) UV-vis diffuse reflectance spectra and corresponding Tauc plots with the estimated band gaps of g-C_3N_4 prepared from thiourea at different temperatures: (b) 400 °C, (c) 440 °C, (d) 500 °C, (e) 550 °C, (f) 600 °C.

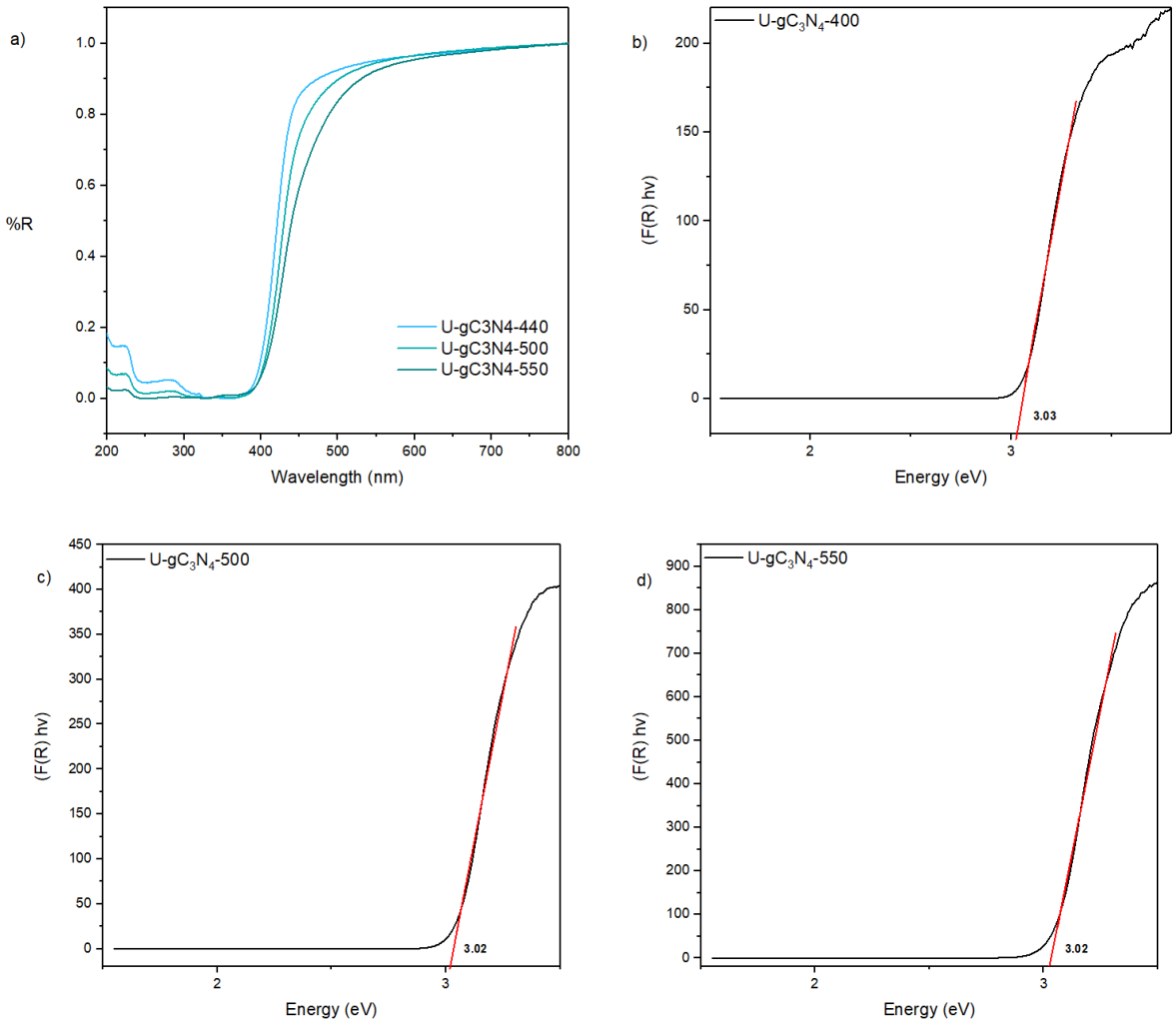

Figure 3.1.3.2. (a) UV-vis diffuse reflectance spectra and corresponding Tauc plots with the estimated band gaps of g-C_3N_4 prepared from urea at different temperatures: (b) 440 °C, (c) 500 °C, (d) 550 °C.

As shown in the Tauc plots reported in **figure 3.1.3.1** and **3.1.3.2**, it is possible to notice an increase in the band gap value compared to the literature value (~2.7 eV [4-15]) both in the case of the samples prepared from thiourea and urea. However, it is possible to appreciate a decrease in the band gap value from the sample at 400 °C to the ones at 440, 500 and 550 °C, as expected from the temperature increase. In particular, in the case of

g-C_3N_4 prepared from thiourea, the band gap energy ranges from 2.98 eV (400 °C) to 2.89 eV (550°C) and increases again at 600°C (2.99 eV). This effect may be due to the strong quantum confinement effects, because high temperatures can induce the thermal decomposition of g-C_3N_4 into smaller particles [12]. The band gap energy of the samples synthesised from urea is even higher, being slightly higher than 3.0 eV. These result support our choice of T-gC_3N_4-550 (B-gC_3N_4) for the successive steps, since it is the one with the lowest band gap energy.

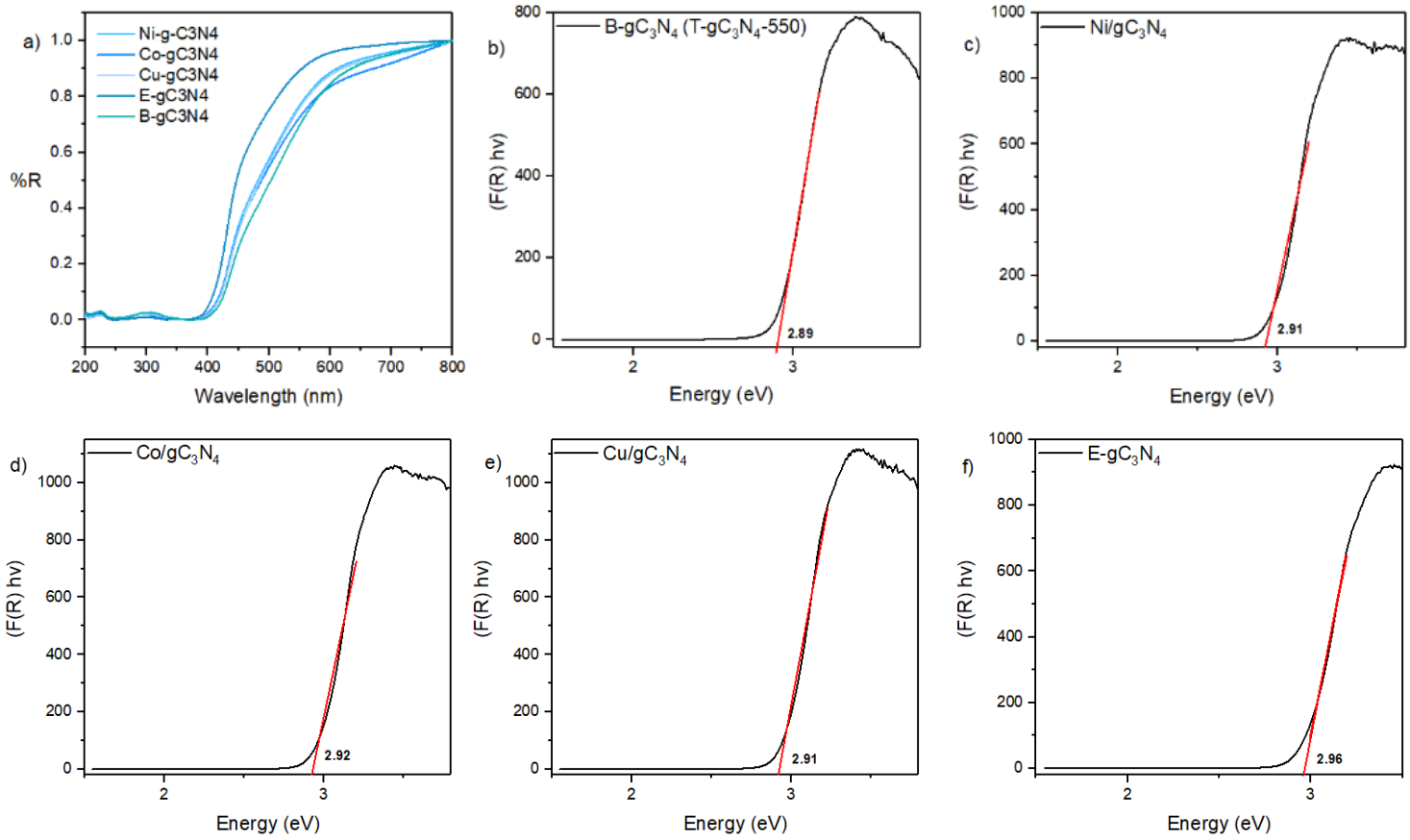

Figure 3.1.3.3. (a) UV-vis diffuse reflectance spectra and corresponding Tauc plots with the estimated band gaps of (b) B-g-C_3N_4, (c) Ni/g-C_3N_4, (d) Co/g-C_3N_4, (e) Cu/g-C_3N_4 and (f) E-g-C_3N_4.

It is interesting to notice that most of the samples prepared from B-g-C_3N_4 show more or less the same band gap value (~2.89 eV), with a slight increase to 2.91 eV in the case of Ni/g-C_3N_4 and Cu/g-C_3N_4 and 2.92 eV for Co/g-C_3N_4. However, these small differences

are probably due to oscillations in the value, rather than significant differences in the optical properties of the materials. From these results it is possible to conclude that the band bag energy was not affected by the successive synthetic steps (doping with metal atoms). Instead, an increase in the band gap value to 2.96 eV occurs in E-g-C_3N_4: this is due to the quantum confinement effect separating the conduction and valence band in opposite directions [15, 17].

3.1.4. Photoelectrochemical measurements

The photoelectrochemical activity of g-C_3N_4 samples toward OER was tested in an Argon-saturated three-electrode system in 0.1M Na_2SO_4. The as-obtained LSV curves are reported below in **figure 3.1.4.1.**

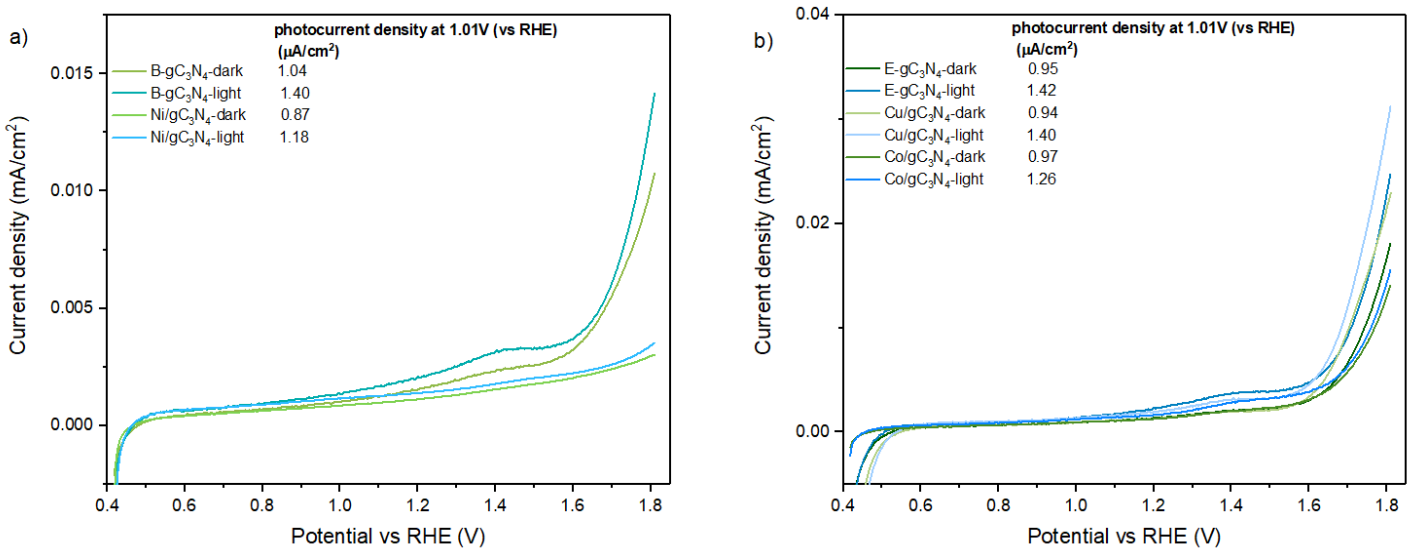

Figure 3.1.4.1. LSV curves of the various samples from 0.4 to 1.81 V (vs RHE) under no light and when exposed to the LED light: a) B-g-C_3N_4, Ni/g-C_3N_4; b) E-g-C_3N_4 and Cu/g-C_3N_4 and Co/g-C_3N_4. The samples were divided according to their scale, to better reproduce the outcomes of the analysis. The values of photocurrent densities at 1.01 V and in both conditions are also reported.

To better evaluate the photon-generated current of the various g-C_3N_4 samples, the values of photocurrent density at 1.01 V were compared with each other. In particular, in the absence of light, the sample with the highest photocurrent density appears to be the B-g-C_3N_4, followed by Co/g-C_3N_4, E-g-C_3N_4, Cu/g-C_3N_4, and Ni/g-C_3N_4, respectively. When exposed to light a rather small improvement in the photocurrent density can be noticed for all the samples. E-g-C_3N_4 showed the highest photocurrent density value (1.42 $\mu A/cm^2$) with a small increase compared to B-g-C_3N_4 and Cu/g-C_3N_4 (1.40 $\mu A/cm^2$) which was then followed by Co/g-C_3N_4 and Ni/g-C_3N_4 (1.26 and 1.18 $\mu A/cm^2$, respectively).

Comparing the photocurrent density values from the different samples it can be concluded that there is a slight improvement in the performance from bulk to exfoliated sample. However, the deposition of single atoms on bulk g-C_3N_4 didn't lead to a strong improvement in the photocurrent density. B-g-C_3N_4 and Cu/g-C_3N_4 show similar values under light exposure, while a decrease is observed in the case of Co and, in particular, of Ni. However, it is interesting to notice that E-g-C_3N_4 exhibited the highest increase in the photocurrent density when exposed to light compared to dark conditions, indicating its increased reactivity to light compared to the other samples. On the contrary, samples like Co/g-C_3N_4 and Ni/g-C_3N_4 show a smaller increase in performance, with Ni/g-C_3N_4 being the worst performing sample. However, it is apparent that the differences in the values of all the samples are rather small, indicating that exfoliation and doping didn't affect the performance hugely. Furthermore, the photocurrent density generation is very small for all the samples, being of the order of $\mu A/cm^2$ rather than mA/cm^2, as reported in the literature. This could be due to slow charge transfer and poor electron-hole pair separation. Other possible reasons could be the preparation of the electrodes and the electrolyte used during the measurements. A neutral electrolyte was used (0.1M Na_2SO_4), while metal doped samples should work better in basic solution (e.g. 1M KOH). For instance, Pattnaik et al. report values of 0.2 and 0.26 mA/cm^2 for bulk and exfoliated under no light condition, while the photocurrent densities are improved to 0.24 and 0.42 mA/cm^2 under light exposure [15]. An increase in the performance is generally reported for metal-doped samples or samples with single metal atoms deposited on them, which is not our case [64,65]. This generally indicates a non-efficient generation and separation of photoinduced electron-hole pairs.

Transient photocurrent response of the g-C_3N_4 samples was also evaluated in condition of light and no light at 1.01V (vs RHE). The outcomes of this analysis are reported below in **figure 3.1.4.2**. The difference between the values of photocurrent density in these two conditions was also computed to better compare and evaluate the experimental data of the different samples since a shift in the current density values of the different samples can be noticed.

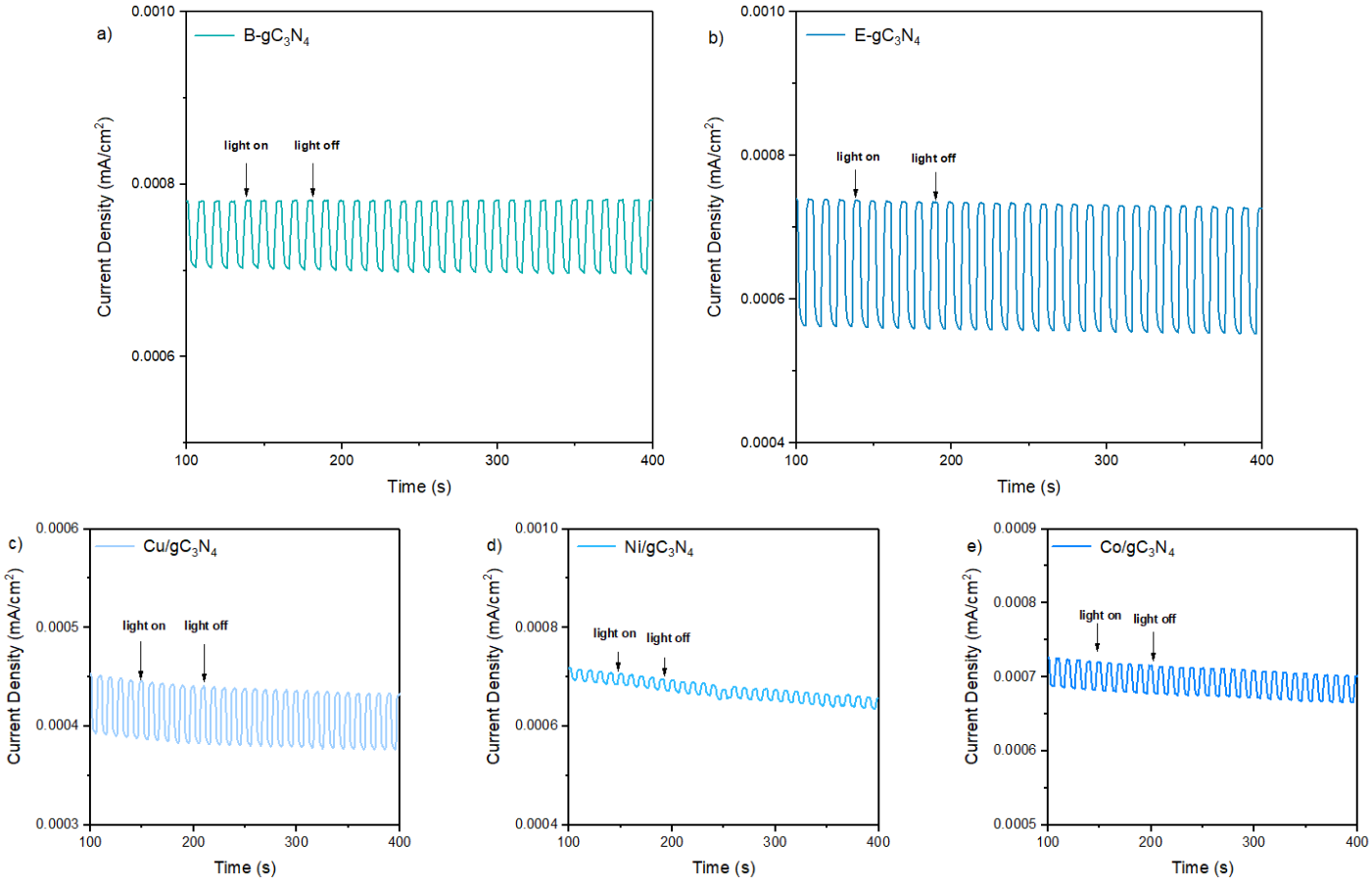

Figure 3.1.4.2. Transient photocurrent response of the various samples at 1.01 V (vs RHE): a) B-g-C_3N_4, Ni/g-C_3N_4 and Co/g-C_3N_4; b) E-g-C_3N_4 and Cu/g-C_3N_4. The samples were divided according to their scale, to better reproduce the outcomes of the analysis.

Table 3.4. Table reporting the photocurrent values recorded with light and without light from the transient photocurrent response plots in **figure 3.1.4.2**, together with the difference between these two values (height).

Transient photocurrent response (PSTAT)

Samples	Light on (μA/cm^2)	Light off (μA/cm^2)	Height (μA/cm^2)
B-g-C_3N_4	0.78	0.7	0.08
E-g-C_3N_4	0.73	0.56	0.17
Ni/g-C_3N_4	0.67	0.65	0.02
Co/g-C_3N_4	0.71	0.67	0.04
Cu/g-C_3N_4	0.44	0.38	0.06

Comparing the values of photocurrent density obtained from PSTAT with the ones from the LSV curves at the same potential (1.01 V), it can be noticed a general decrease in the values recorded by PSTAT compared to the ones from LSV for all the samples. This can be explained by the fact that potentiostatic measurements were taken after LSV and therefore some degradation or oxidation of the film of the electrode probably occurred. Comparing the intensities of the PSTAT, therefore the increase in the photocurrent density from no light condition to light exposure, from the different samples it can be concluded that there is an improvement in the performance from the bulk to exfoliated sample (0.08 and 0.17 μA/cm^2, respectively). On the contrary, the deposition of single atoms didn't lead to an improvement in the intensity of the photocurrent density compared to B-g-C_3N_4. The intensity decreases in fact from Cu/g-C_3N_4 (0.06 μA/cm^2) to Co/g-C_3N_4 (0.04 μA/cm^2) and finally to Ni/g-C_3N_4 (0.02 μA/cm^2). Therefore, the intensity values of B-g-C_3N_4 and Cu/g-C_3N_4 are quite similar, while it decreases in the case of Co/g-C_3N_4 and, in particular, of Ni/g-C_3N_4. Furthermore, in the case of these last two samples, it can be noticed a decrease in the current density with time, in particular in the case of Ni-doped sample. This, therefore, indicates poor stability and gives information on trapping and/or recombination processes [65]. So, these results are generally in agreement with those reported from LSV under light exposure, confirming that the exfoliated sample is the one that shows the best reactivity to light, while Ni/g-C_3N_4 is the worst performing one. Higher photocurrent densities are associated with faster-photogenerated charge transfer dynamics. This means that the charge transfer is rather slow in the case of the synthesised samples. In particular, in the case of the metal-doped samples it seems that the charge transfer is similar or even lower (like for Ni) than the bulk one.

EIS measurements at 1.21 V (vs RHE) were also performed to better investigate the charge transfer kinetics occurring at the sample-solution interface.

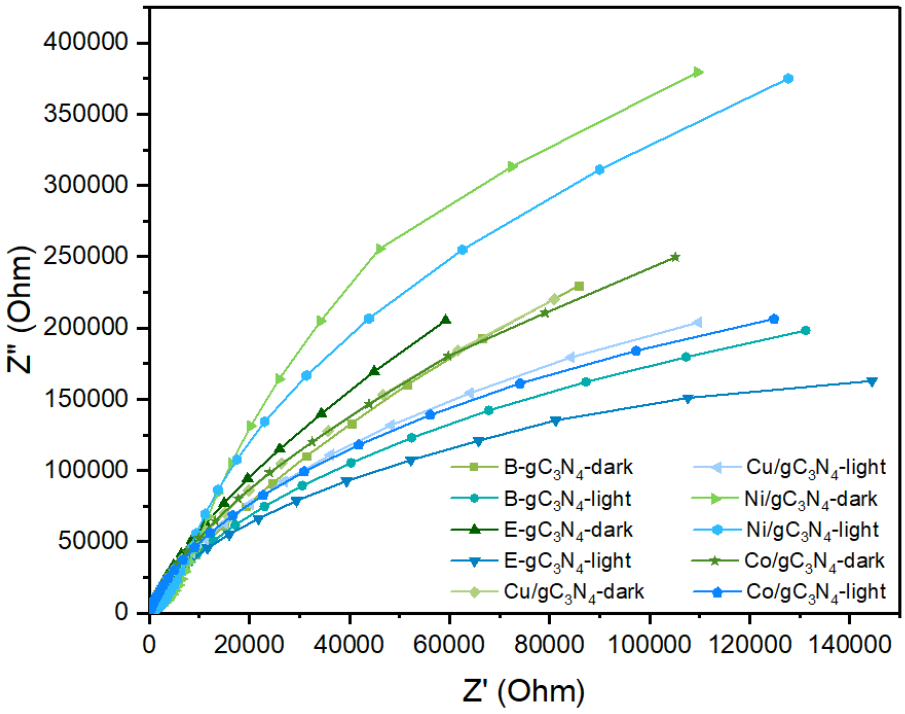

Figure 3.1.4.3. Nyquist plots of B-g-C_3N_4, E-g-C_3N_4, Ni/g-C_3N_4 and Co/g-C_3N_4 and Cu/g-C_3N_4 samples in light and no light conditions.

The results of the Nyquist plots are almost in accordance with the previous analysis (LSV curves and transient photocurrent response) since a higher resistance value is expected in the case of samples with lower photocurrent densities and vice versa. In particular, samples from lowest to highest resistance in the light are reported as follows: E-g-C_3N_4, B-g-C_3N_4, Co/g-C_3N_4, Cu/g-C_3N_4 and finally Ni/g-C_3N_4. These results reflect the outcomes of the previous measurements. Furthermore, a much lower resistance of the exfoliated sample compared to the bulk one is in agreement with what was reported by the literature [15]. The resistance of Cu/g-C_3N_4 under light exposure is slightly higher than the one of the Co-doped sample, while it showed a higher photocurrent, but the difference seems very small. In no light condition the highest resistance is recorded for Ni/g-C_3N_4, as expected, followed by E-g-C_3N_4 and then by Co/g-C_3N_4, B-g-C_3N_4 and Cu/g-C_3N_4 with highly similar values. So, it can be concluded that the results obtained from EIS analysis are comparable with the ones produced by the previous measurements. However, it has to be noted that no semicircle typical of this kind of analysis was obtained, translating in very high resistances, much higher than literature [15]. This

indicates very slow charge transfer and poor electron-hole pair separation but it could also be due to the preparation of the electrodes and the electrolyte used during the measurements, as mentioned before. However, this is consistent with the fact that the photocurrent generated by the samples is very small being of the order of $\mu A/cm^2$.

Among the possible reasons behind the poor photoelectrochemical performance, the most significant factors can be poor charge separation, low electronic conductivity and small diffusion length. Charge diffusion length is important in terms of charge separation, migration and surface reactions. Charge separation and recombination are affected by the presence of trap states in the material: if electrons are trapped by acceptors in the material (in the case of this work, g-C_3N_4), they remain inactive and do not participate in photoelectrochemical reactions, thus lowering the performance. These trap states can be introduced by structural disorder and/or presence of defects in the sample and they can prohibit the directional charge transfer (which is vital in a PEC system) affecting the charge diffusion length [66]. Consequently, bulk samples have more structural disorder and defect density which result in deep trap states and reduced performance. This may explain the poor performance recorded for the samples of this thesis. As for the metal-doped samples, it is important to consider that the metal atoms were deposited on bulk g-C_3N_4 and the presence of the bulk structure was confirmed by morphological analysis. Therefore, a high amount of defects may be present as well, which can act as traps for electrons. Furthermore, no significant differences among the samples could be noticed from UV-vis analysis and band gap values. This could suggest that the deposition of metal elements did not improve the structural and electrical properties, and therefore could explain why the performance did not improve [67]. Moreover, in absence of characterization techniques that could confirm the presence of metals as single atoms, it would be possible to hypothesize a partial agglomeration, leading to the occupation of active sites and reduction of electron mobility [64].

3.2 LDH samples

This paragraph discusses the results of the structural and morphological characterizations (X-ray diffraction, scanning electron microscopy, energy-dispersive spectrometry and Raman spectroscopy) and electrochemical water splitting performed on the LDH samples.

3.2.1 XRD analysis

The diffraction patterns of the samples NiCo_1:1.26 and NiCo_1:2 have been analysed to verify their crystalline structure. They are reported together with the reference pattern in the following figure (**figure 3.2.1.1**).

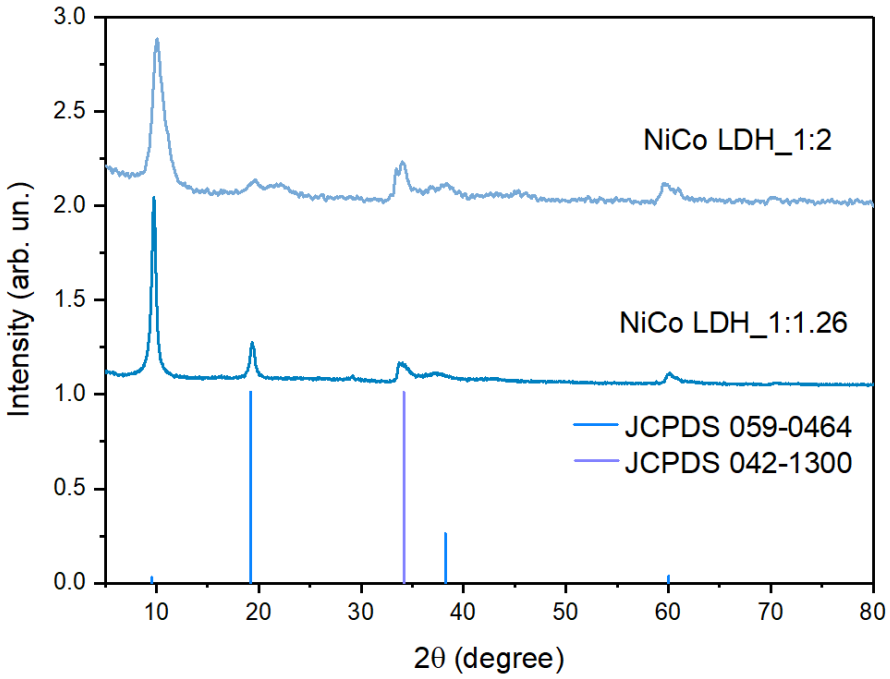

Figure 3.2.1.1. XRD patterns of NiCo_1:1.26 and NiCo_1:2 (from bottom to top) compared to the reference patterns provided by the software (JCPDS 059-0464 and 042-1300).

Table 3.2.1. Table reporting the position of the peaks from the patterns reported in **figure 3.2.1.1.** together with the corresponding crystallographic planes.

Peaks (° of 2θ)		XRD planes
NiCo_1:1.26	**NiCo_1:2**	
9.8	10.1	(001)
19.4	19.4	(002)
33.9	33.9	(111)
37.3	37.8	(201)
60.1	59.8	(006)

The XRD patterns of the two samples of NiCo LDH analyzed display a similar structure to the ones usually found in the literature [63, 64], with main peaks indicated approximately at around 10, 20, 34, 38 and 60°. Analysis at the software provides two reference patterns JCPDS 059-0464 and 042-1300, belonging to phases NiO(OH) and CoO, thus indicating that the samples are a mixed phase. In particular, the phase NiO(OH) corresponds to a monoclinic crystal system with space group C12/m1 and space group number 12, while the phase CoO is associated with a cubic system with space group F-43m and space group number 216. The phases obtained are therefore different from the ones usually reported in the literature for this kind of system (α- or β-$Ni(OH)_2$ and $Co(OH)_2$). In particular, NiO(OH) is an oxidised form of β-$Ni(OH)_2$. The conversion occurs upon the removal of a proton and an electron and the obtained structure is less ordered than that of β-$Ni(OH)_2$. Furthermore, the removal of the proton leads to an increased electrostatic repulsion, which in turn leads to a decrease of the unit cell parameter from 3.12 to 2.82 Å, due to reduced Ni-Ni distance, and to an increase in the interlayer distance (c=4.85 Å). CoO is an oxidised form of $Co(OH)_2$ which can be produced by dehydration of the hydroxide. It can be noticed that the intensity of some of the peaks in the experimental data is different from the ones of the references. For instance, the peaks located at ~10° are more intense than the one of the reference, while the one at ~19 and 34° are less intense. Variation in the intensities of the peaks could be due to differences in the orientation of the crystallites. The peaks with the highest intensity

are generally associated with the planes that are more exposed to the radiation, while the less exposed ones display lower intensity. Therefore, it can be concluded that the crystallites of the samples were oriented in a different way compared to the ones inserted in the software and used as a reference, with planes in the samples being more exposed than the ones in the reference and vice versa.

Comparing the patterns of the two samples, the positions of the peaks are very similar to each other, thus suggesting that the crystalline structure was not affected by the change in the molar ratio between metals. On the other hand, some of the peaks in the pattern of NiCo_1:2 seem widened compared to the ones of NiCo_1:1.26. This might suggest that the crystallites of NiCo_1:2 are smaller than the other sample.

3.2.2 SEM and EDS analysis

SEM images of NiCo_1:1,26, NiCo_1:2, Pt/NiCo_1:1,26, Pt/NiCo_1:2, Ru/NiCo_1:1,26 and Ru/NiCo_1:2 were taken in order to study their morphology, while their elemental composition was investigated through EDS. EDS spectra, together with corresponding elemental mapping images, are reported in the following figures from **figure 3.2.2.1** to **3.2.2.5**. The tables provide an estimate of the ratios in atomic percentage concentration.

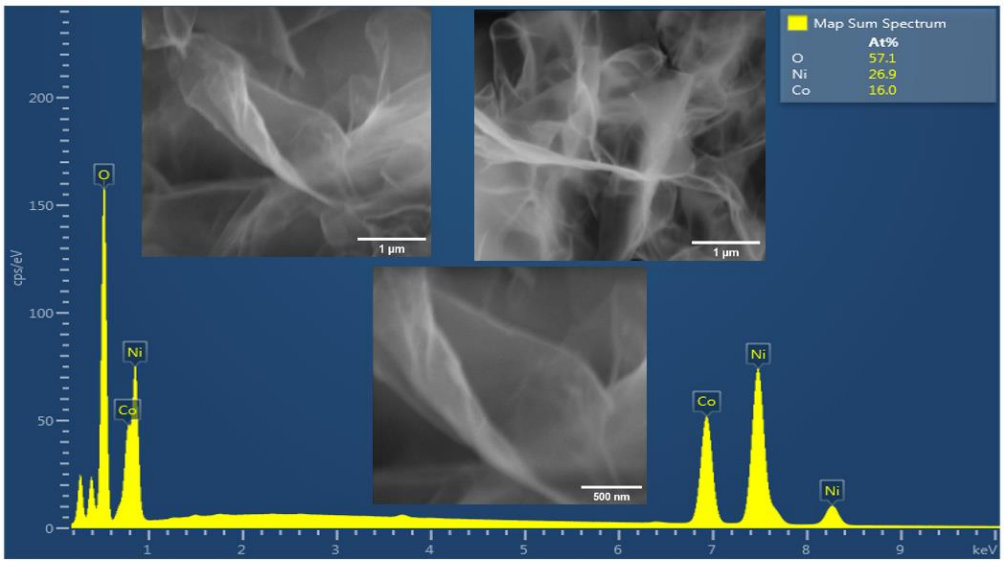

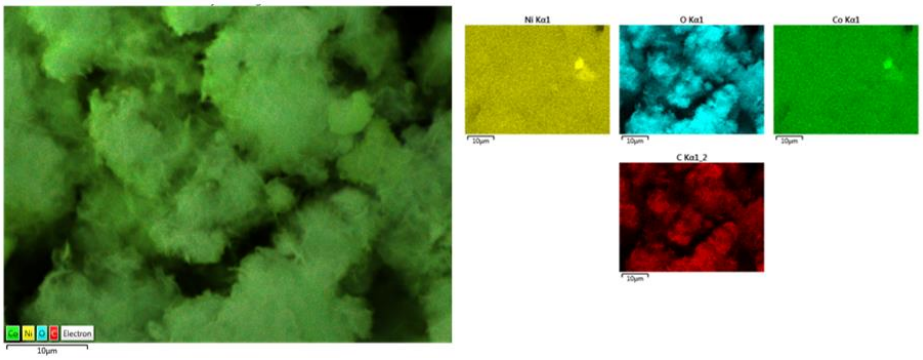

Figure 3.2.2.1. SEM images (in the inset) and EDS spectrum and elemental mapping of NiCo_1:1,26.

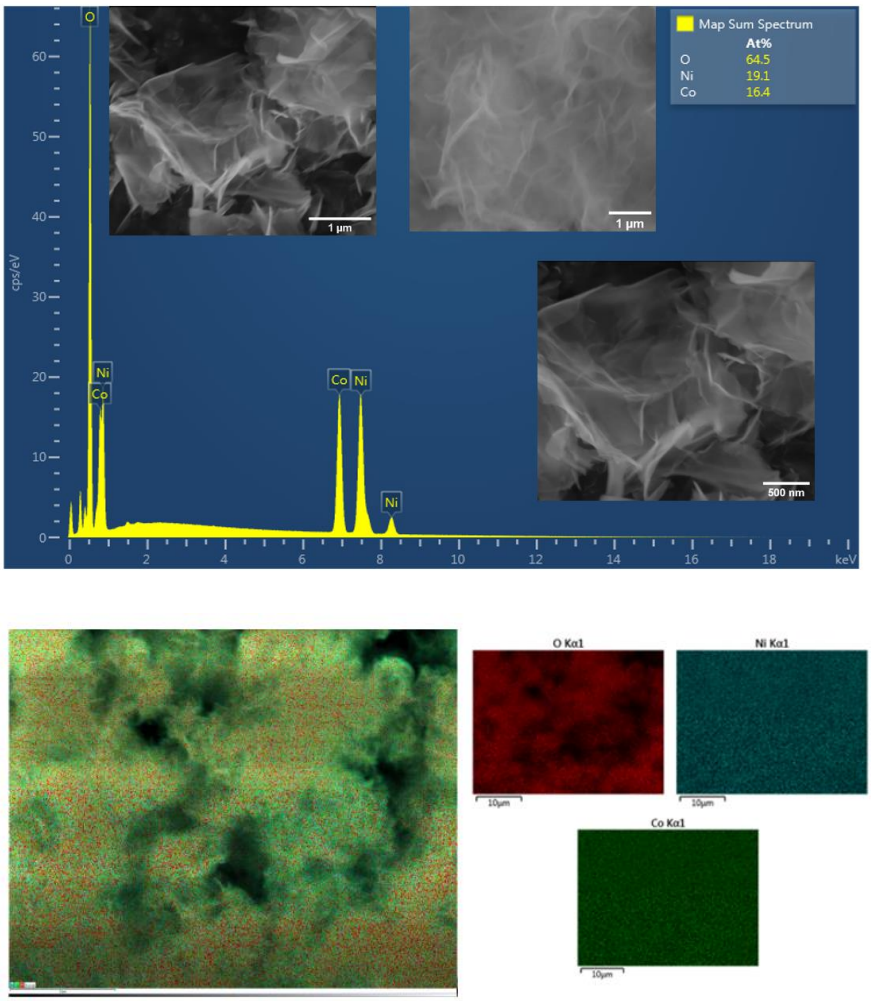

Figure 3.2.2.2. SEM images (in the inset) and EDS spectrum and elemental mapping of NiCo_1:2.

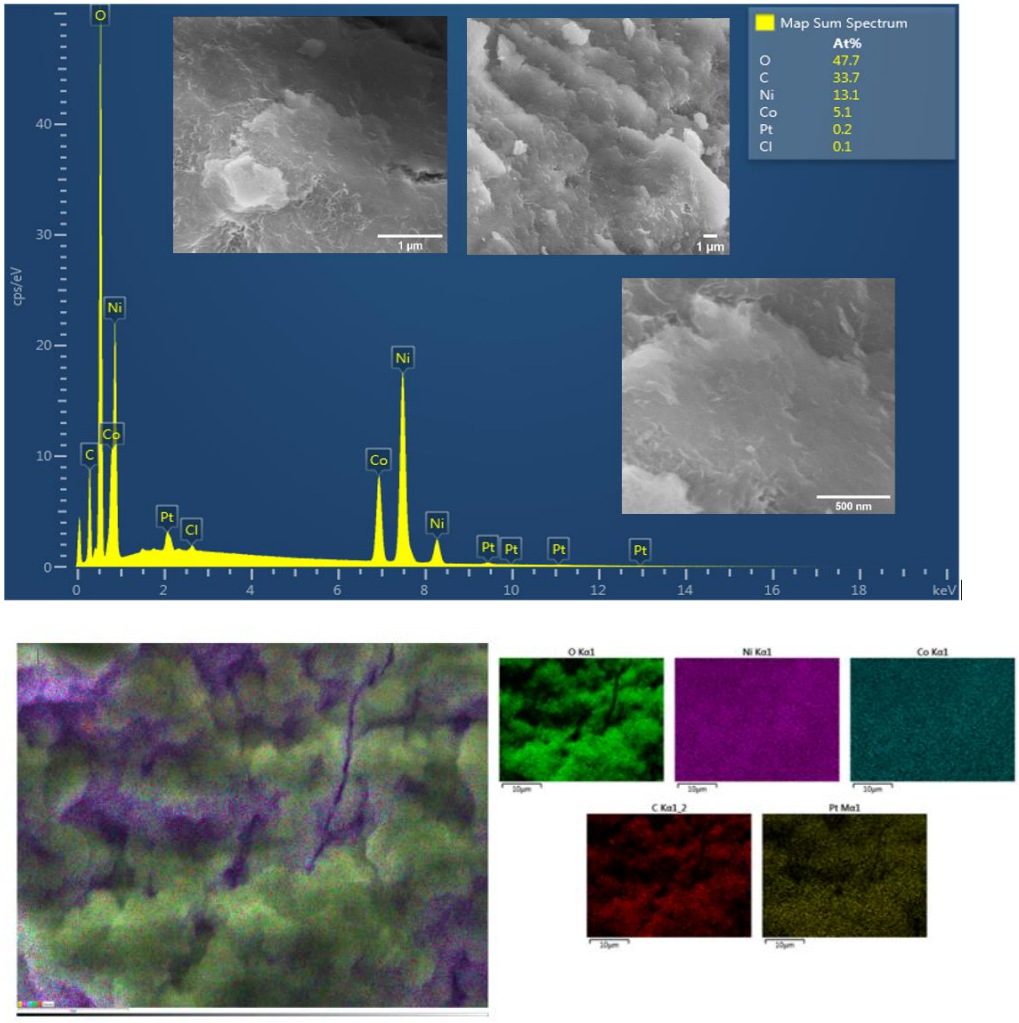

Figure 3.2.2.3. SEM images (in the inset) and EDS spectrum and elemental mapping of Pt/NiCo_1:1,26.

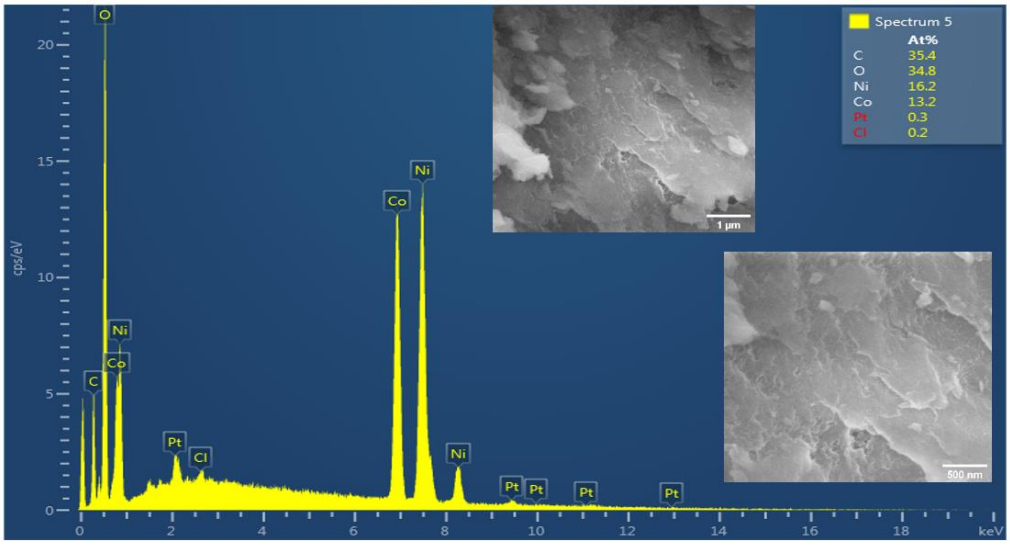

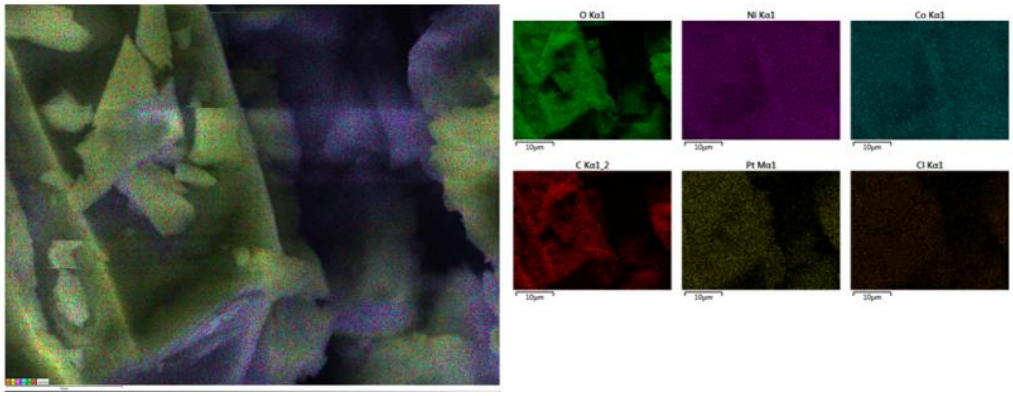

Figure 3.2.2.4. SEM images (in the inset) and EDS spectrum and elemental mapping of Pt/NiCo_1:2.

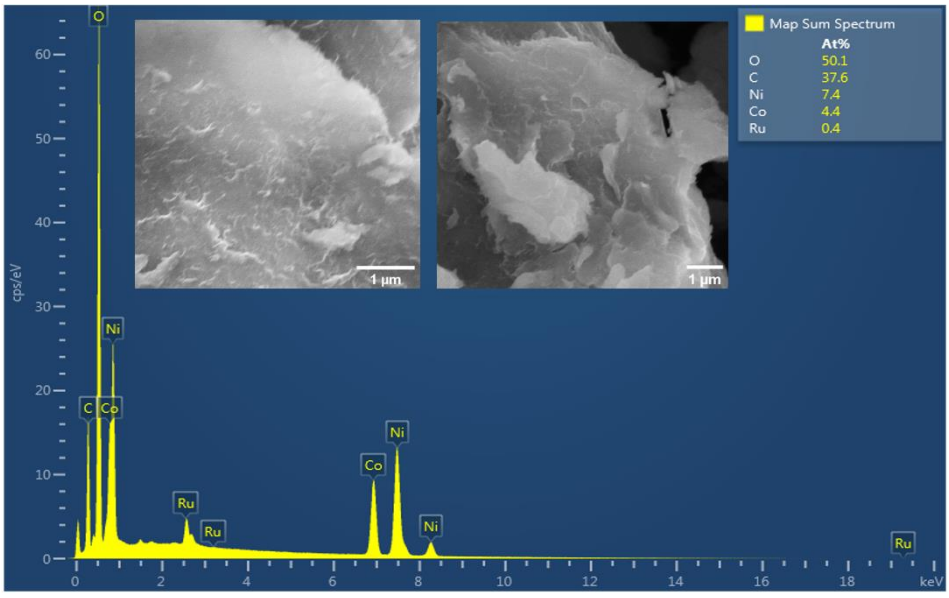

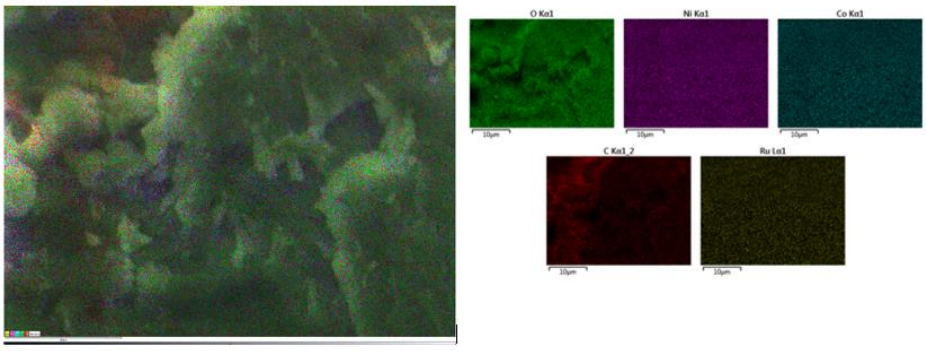

Figure 3.2.2.5. SEM images (in the inset) and EDS spectrum and elemental mapping of Ru/NiCo_1:1,26.

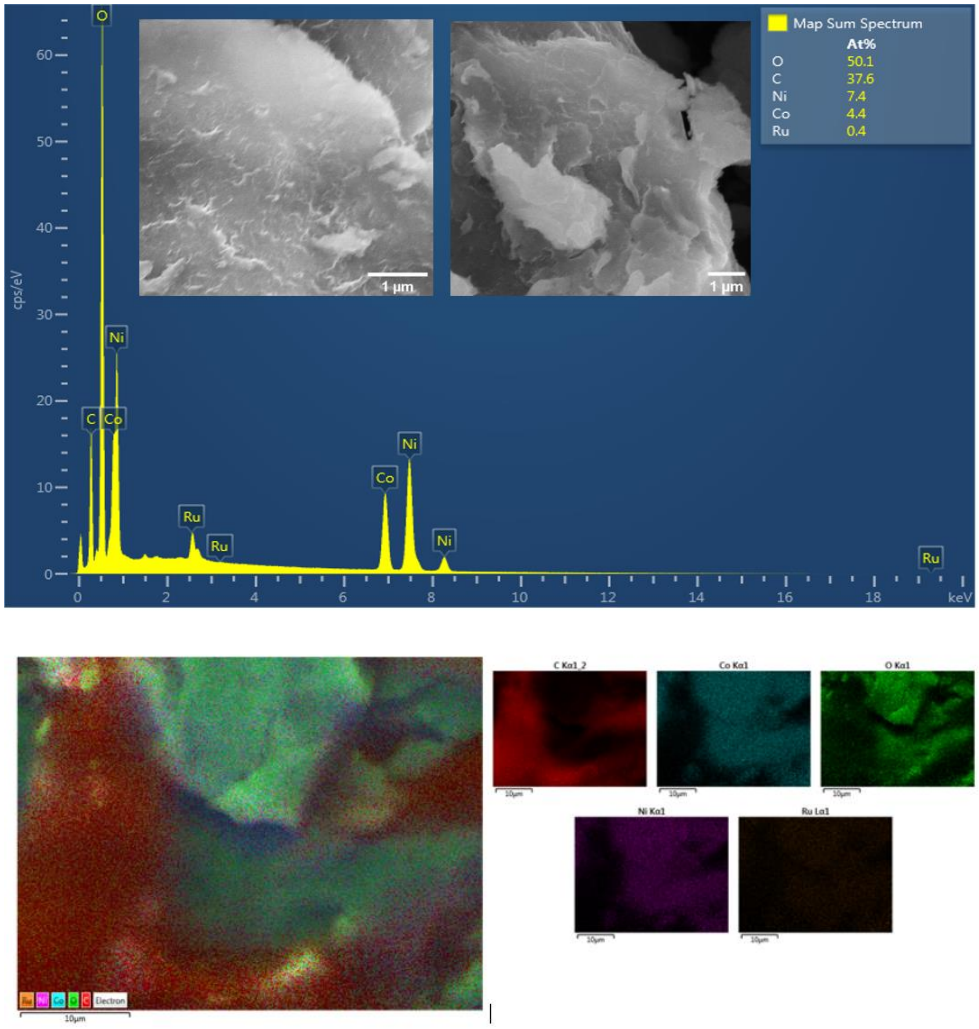

Figure 3.2.2.6. SEM images (in the inset) and EDS spectrum and elemental mapping of Ru/NiCo_1:2.

The SEM images of NiCo_1:1,26 and NiCo_1.2 show a uniform morphology in the samples. Both are constituted by nanosheets, which appear to be very thin. On the contrary, in the SEM images of Pt/NiCo_1:1.26, Pt/ NiCo_1:2, Ru/NiCo_1:1.26 and Ru/ NiCo_1:2 it is not possible to identify clearly thin nanosheets. However, the presence of structures recalling nanosheets but "attached" to the structure can be noticed. It is, therefore, possible to hypothesize that the addition of the metal is the factor that affected the morphology: this might be since it "grasps" most of the urea, which is responsible for the formation of the LDH structure and is then not available to Ni and Co. However, it is not possible to have evidence of the presence of Pt and Ru, not even as nanoparticles, in the samples in the SEM images, which are instead detected by EDS analysis and

elemental mapping. To verify if such elements are deposited as single atoms, other characterization techniques should be employed, including HAADF-STEM and STM. EXAFS and XANES could instead provide information on the electronic and geometrical structure of the metal species.

The EDS spectra confirm the presence of Ni and Co in all the samples, as expected from the synthetic procedure. However, it is possible to notice a very intense peak due to oxygen: this might be due to air, the presence of water in the samples or leftover urea, which was one of the precursors during the synthesis. Furthermore, the EDS spectra of Pt/NiCo_1:1.26, Pt/NiCo_1:2, Ru/NiCo_1:1.26 and Ru/NiCo_1:2 report the presence of Pt and Ru in the samples, thus suggesting a positive outcome from single-atom catalysis. In all the samples with metal atoms deposited on them, it is possible to observe a uniform distribution of Pt or Ru in the EDS mapping. However, EDS does not allow us to understand whether they are deposited as single atoms.

3.2.3. Raman spectroscopy

Raman spectroscopy was performed on all the LDH samples to confirm their chemical structure. Raman spectra are reported in the following figure (**figure 3.2.3.1**).

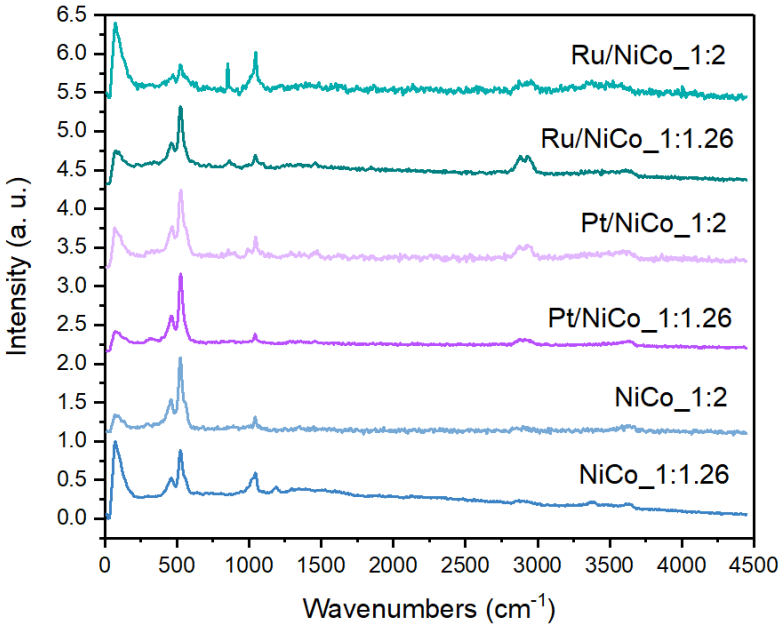

Figure 3.2.3.1. Raman spectra of NiCo_1:1.26, NiCo_1:2, Pt/NiCo_1:1.26, Pt/NiCo_1:2, Ru/NiCo_1:1.26 and Ru/NiCo_1:2 (from the bottom to the top).

In the Raman spectra of all samples it is possible to notice the presence of two peaks ~460 and ~520 cm^{-1}: they are typical of NiCo LDH and are associated with Ni-O and Co-O vibration modes respectively [69]. This further supports the fact that the structure of the synthesised samples is the expected one. In particular, they are located at 458 and 520 cm^{-1} in the case of NiCo_1:1.26 and NiCo_1:2, while they are shifted to 464 and 526 cm^{-1} in the case of Pt/NiCo_1:1.26, Pt/NiCo_1:2, Ru/NiCo_1:1.26 and Ru/NiCo_1:2. In the spectra other peaks are also present. The one at 1055 cm^{-1} in NiCo_1:1,26 and 1043 cm^{-1} in all the other samples is probably caused by the laser power: it oxidizes the sample thus generating this signal. This hypothesis is supported by the fact that, as the laser power increases, the intensity of the peak increases as well and vice versa. The peaks centred at 3372 and 3625 cm^{-1} in NiCo_1:1,26, 2898 and 3630 cm^{-1}in NiCo_1:2, Pt/NiCo_1:1,26 and Pt/NiCo_1:2, 2900 and 3618 cm^{-1} in Ru/NiCo_1:1,26 and 2916 and 3464 cm^{-1} in Ru/NiCo_1:2 could be assigned to the stretching of C-H and O-H, respectively, since they are usually located between 2800-3300 and 3300-3600 cm^{-1} and the presence of these elements is confirmed by the EDS analysis reported in paragraph 2.3. Unfortunately, normal Raman spectroscopy does not allow to be applied on SACs due to its low sensitivity, allowing to monitor only structural information of the bare catalyst [70].

3.2.4 Electrochemical measurements

The electrochemical activity of LDH samples toward OER was tested in an Argon-saturated three-electrode system in 1M KOH. The polarization curves of the samples, together with the corresponding Tafel plots, are reported in **figure 3.2.4.1.** The kinetics of OER activity was also evaluated by considering the Tafel slopes derived from the Tafel plots.

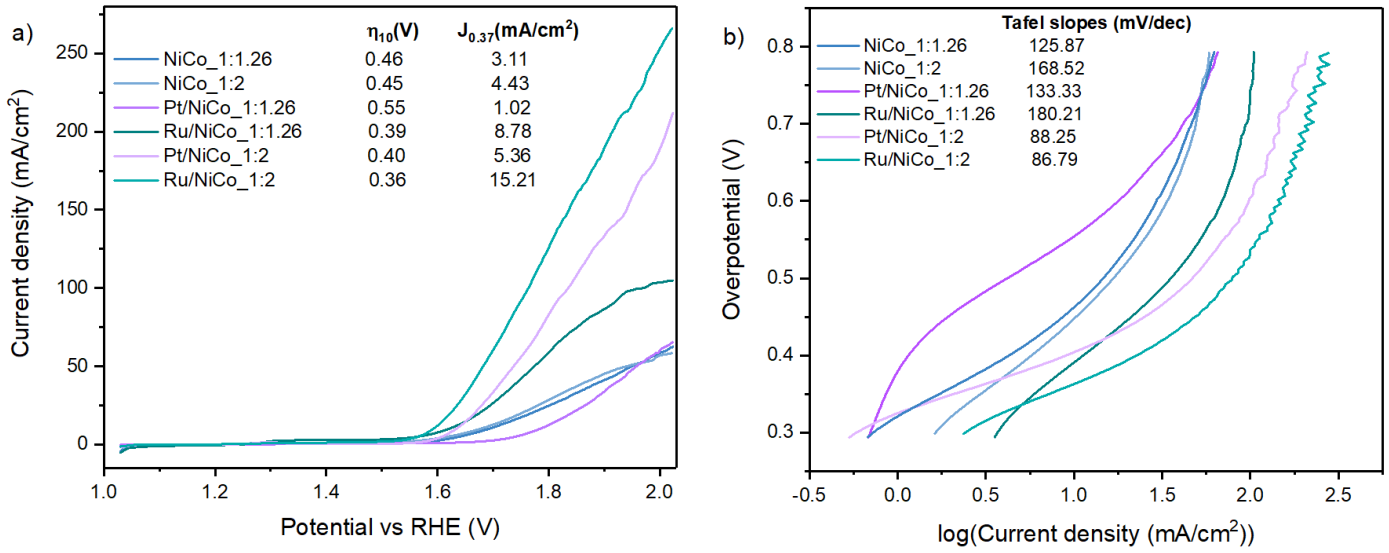

Figure 3.2.4.1. (a) Polarization curves of NiCo_1:1.26, NiCo_1:2, Pt/NiCo_1:1.26, Ru/NiCo_1:1.26, Pt/NiCo_1:2 and Ru/NiCo_1:2 from 1.02 to 2.02 V (vs RHE). The values of overpotential η_{10} at 10 mA/cm^2 and of current density at 2.02 V are also reported. (b) Corresponding Tafel plots and slopes.

To evaluate the electrochemical activity toward OER of the different LDH samples, the values of current density $J_{0.37}$ at an overpotential of 0.37 V (corresponding to the onset potential) were compared with each other. In particular, it can be noticed that the samples of NiCo_1:1.26 and 1:2 are among the ones with the lowest current densities (3.11 and 4.43 mA/cm^2, respectively), as expected due to the absence of deposited metal atoms. Furthermore, the two samples have similar current density values, thus suggesting that different molar ratios, therefore the increased amount of Co in NiCo_1:2 sample, didn't improve hugely the catalytic performance in this case. As for the samples with Pt deposited on them, Pt/NiCo_1:1.26 has a lower current density than that of the samples without any metal atoms (1.02 mA/cm^2), which is different from expectations since the deposition of metals as single atoms should improve the current density. An increase in the current density value is instead reported in the case of Pt/NiCo_1:2 (5.36 mA/cm^2), so much higher than Pt/NiCo_1:1.26. This could be ascribed to both the presence of Pt and the different molar ratio of the support (1:2). Taking into account samples containing Ru atoms, an improvement in their performance can be observed for both

Ru/NiCo_1:1.26 and Ru/NiCo_1:2 (8.78 and 15.21 mA/cm^2, respectively) compared to samples without metals. In particular, Ru/NiCo_1:2 exhibits a higher current density value, more than the triple of NiCo_1:2 and almost the double of Ru/NiCo_1:1.26, thus suggesting again that the choice of the molar ratios is a significant parameter for the final performance of the samples and that better results can be achieved with molar ratio 1:2 [63]. The values of overpotential η_{10} at 10 mA/cm^2 were also chosen as a parameter to compare the performance of the samples. They reflect the trend in the value of current density at 0.37 V reported above: lower overpotential values are recorded for the samples with higher current density values and vice versa. In particular, the lowest one correspond to Ru/NiCo_1:2 (0.36 V), as expected, then it increases in the following order: Ru/NiCo_1:1.26 and Pt/NiCo_1:2 (similar value: 0.39 and 0.40 V, respectively), NiCo_1:2 and NiCo_1:1.26 (similar values: 0.45 and 0.46 V, respectively) and Pt/NiCo_1:1.26 (0.55 V). The values obtained are slightly higher than values reported by authors in the literature. For instance, Qin et al. [68] and Song et al. [28] report a value of overpotential of ~0.388 V for NiCo LDH without metals. The values of the Tafel slopes derived from the Tafel plots generally follow the trend of the previous parameters. Samples with lower current density display higher Tafel slopes: for instance, NiCo_1:1.26, Pt/NiCo_1:1.26 and NiCo_1:2 show Tafel slopes of 125,87, 133,33 and 168,52 mV/dec, respectively. Ru/NiCo_1:1.26 exhibits a higher slope than expected, considering that it had a higher current density than the previous samples. On the contrary, lower Tafel slopes are recorded for Pt/NiCo_1:2 and Ru/NiCo_1:2: 88.25 and 86.79 mV/dec, respectively. This is expected since a lower Tafel slope for samples with higher current density should be obtained. The values of the obtained Tafel slopes seem quite high if compared to the literature. For instance, a slope of 65 mV/dec was obtained by Song et al. [28] for bulk NiCo LDH. However, also higher and contrasting values are also reported (e.g. 104.7 mV/dec by Fan et al. [69] and 247.6 mV/dec by Qin et al. [68]).

In conclusion, it is generally confirmed that the deposition of metal atoms can improve the performance, since this kind of sample shows higher current density values at 0.37 V and lower overpotentials at 10 mA/cm^2 than the ones without metal. In particular, samples with Ru perform better than Pt. Comparing the two molar ratios used, only a small difference can be observed between the two samples without metal atoms (as already

mentioned). In the case of the other samples, those with a molar ratio of 1:2 have higher current density values.

The other two very useful parameters to compare the activity of the different electrocatalysts are the double layer capacitance C_{dl} and the electrochemical surface area ECSA, which are directly related to each other and derived from cyclic voltammetry data, as described in paragraph 2.7.

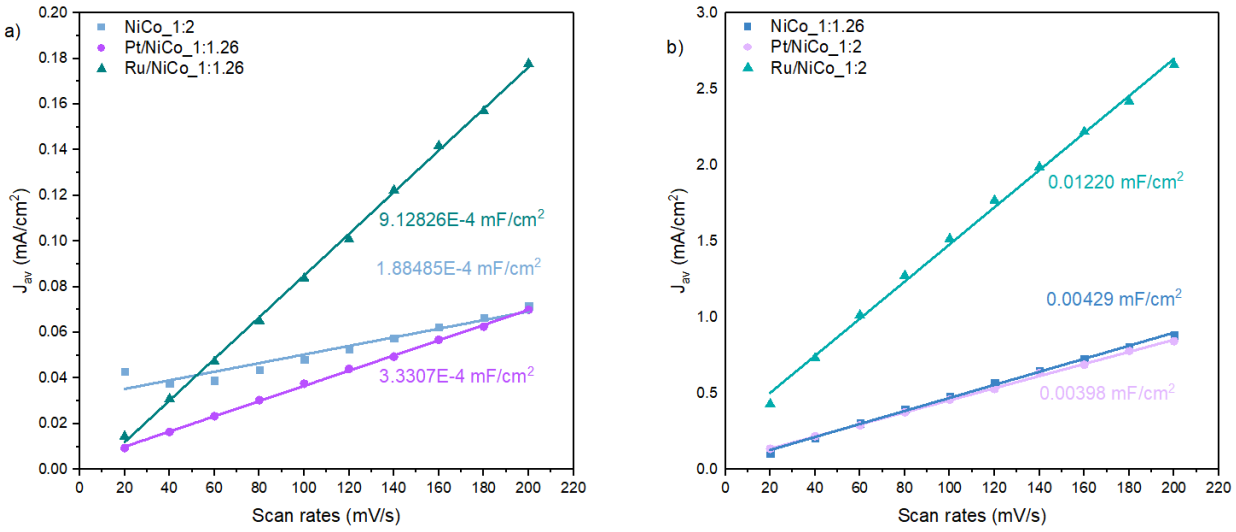

Figure 3.2.4.2. Double layer capacitance (C_{dl}) of a) NiCo_1:2, Pt/NiCo_1:1.26, Ru/NiCo_1:1.26 and b) NiCo_1:1.26, Pt/NiCo_1:2 and Ru/NiCo_1:2. The data were divided according to their scale.

Table 3.2.2. Table reporting C_{dl} and ECSA values of all the samples.

Sample	**C_{dl} (µF/cm^2)**	**ECSA (cm^2)**
NiCo_1:1.26	4.290	0.107
NiCo_1:2	0.190	0.005
Pt/NiCo_1:1.26	0.330	0.008
Ru/NiCo_1:1.26	0.910	0.023
Pt/NiCo_1:2	3.980	0.100
Ru/NiCo_1:2	12.200	0.305

The values of C_{dl} derived from CV and reported in the plots above (**figure 3.2.4.2**) generally agree with the outcomes of the LSV plots, since higher C_{dl} is expected for higher current densities. A high value of C_{dl} may indicate a high density of reactive sites for adsorption and facilitate charge transfer, thus promoting catalytic activity. NiCo_1:1.26 has C_{dl} and ECSA values are a bit higher than expected considering its LSV curve and overpotential value. On the contrary, the values of the two parameters increase accordingly to the current density values derived from the polarization curves, eventually reaching the highest values in the case of Ru/NiCo_1:2 as expected. Comparing the values for samples with the same molar ratio, it is possible to notice an increase from the ones with Pt deposited to the ones with Ru. Taking into account the samples with Pt, values are higher for Pt/NiCo_1:2 than Pt/NiCo_1:1.26. The same can be noticed for the samples containing Ru. This confirms the previous considerations: Ru performs better than Pt and 1:2 is the best molar ratio. The values obtained seem to be lower than what could be expected by considering the literature. For instance, Qin et al. [68] reported a C_{dl} value of 0.0067 mF/cm^2 for NiCo LDH, thus higher than most of the as-synthesized samples.

EIS measurements at 1.62 V (vs RHE) were also performed to better investigate the charge transfer kinetics occurring at the sample-solution interface.

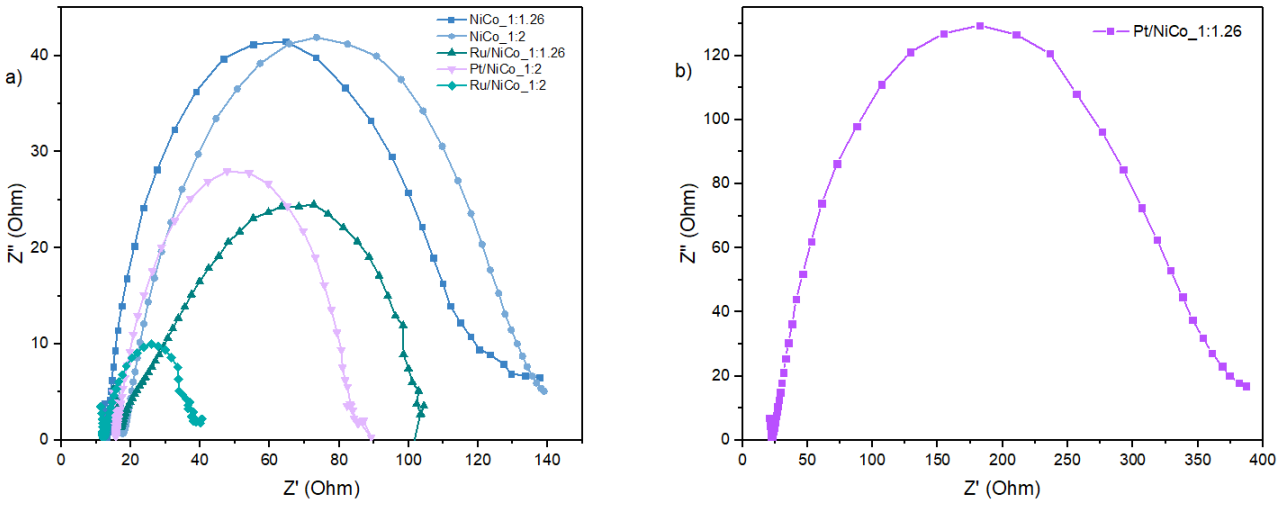

Figure 3.2.4.3. Nyquist plots of NiCo_1:1.26, NiCo_1:2, Ru/NiCo_1:1.26, Pt/NiCo_1:2, Ru/NiCo_1:2 (a) and Pt/NiCo_1:1.26 (b). The data were divided according to their scale.

The results of the Nyquist plots are almost in accordance with the previous analysis (LSV plots and C_{dl} computed from the CV) since a higher resistance value is expected in the case of samples with lower current densities, in our case NiCo_1:2, NiCo_1:1.26 and Pt/NiCo_1:1.26. On the other hand, a decrease in the resistance should occur as the current density value increases. From the plots it appears that Pt/NiCo_1:1.26 has the highest resistance, followed by NiCo_1:1.26 and NiCo_1:2, Ru/NiCo_1:1.26, Pt/NiCo_1:2 and Ru/NiCo_1:2 in descending order. The very high resistance of Pt/NiCo_1:1.26 compared to the other samples could be explained by considering its overpotential at 10 mA/cm^2 (0.55V), which is the highest among the other samples.

As mentioned in previous paragraphs, the performance of the samples strongly depends on their structural, morphological and electronic properties. Therefore, different factors have to be considered also in the case of the LDH samples to explain their lower performance. For instance, the phase conversion to NiO(OH) and CoO from the respective hydroxides may have led to a less ordered structure, different from the stacked structure typical of layered double hydroxides. As mentioned for g-C_3N_4 samples, the higher structural disorder can result in trapping processes and reduced performance. As for Pt/NiCo_1:1.26, the lower performance compared to the other metal-doped samples could find an explanation in a possible agglomeration or uneven distribution of atoms that occurred during the synthesis that could reduce the mobility of the electrons. Another possible reason is that Pt as a co-catalyst is not that stable for OER in basic environment. Furthermore, from SEM analysis it became clear that the layered structure was not preserved upon the addition of metal elements. This may suggest that the improved performance of Ru/NiCo_1:1.26, Pt/NiCo_1:2 and Ru/NiCo_1:2 is improved only by the presence of metal atoms on them (probably with a more even distribution), that could increase the number of active sites, and by the choice of molar ratios. It has been reported that an increased concentration of Co in NiCo LDH can increase the conductivity [63].

4. Conclusions

The aim of this research work was the synthesis of 2D materials, in particular graphitic carbon nitride (g-C_3N_4) and layered double hydroxides (LDH), thanks to the unique properties. Single atom catalysis on both classes of materials was explored to verify if their catalytic performance could be improved. In particular, selected non-noble transition metals (Ni, Co, Cu) were deposited on g-C_3N_4, while selected precious metals (Pt and Ru) were deposited on LDH. The as-synthesized g-C_3N_4-based samples were tested for photoelectrochemical OER (oxygen evolution reaction), while LDH-based samples for electrochemical OER, to investigate their applicability in these reactions.

As for the g-C_3N_4-based systems, the first samples synthesized from thiourea and urea were prepared at different temperatures, to identify the best procedure for the development of g-C_3N_4. The phase obtained was confirmed to be the one of graphitic carbon nitride (space group P21212) for all the samples. The bandgap values of the samples synthesized from thiourea and urea are both slightly higher than those reported in the literature (~2.7 eV), with T-gC_3N_4-550 (B-gC_3N_4) being the one with the lowest band gap energy (2.89 eV). Also in the case of E-g-C_3N_4, Ni/g-C_3N_4, Co/g-C_3N_4 and Cu/g-C_3N_4 (prepared from this last sample), the phase was that of graphitic carbon nitride (space group P21212). SEM micrographs confirmed what emerged from analysis of XRD peaks width: B-g-C_3N_4, Ni/g-C_3N_4, Co/g-C_3N_4 and Cu/g-C_3N_4 possess a bulk structure, with the presence of some aggregates, particularly in the case of B-g-C_3N_4, while a less stacked structure with clearly distinguishable nanosheets was observed for E-g-C_3N_4 due to the exfoliation process. EDS analysis and elemental mapping managed to confirm the expected composition of all the samples, including the presence of Ni, Co and Cu. However, to verify if such elements are deposited as single atoms, other characterization techniques should be employed, including HAADF-STEM and STM. Other elements due to the deposition of the samples on FTO glass and leftovers from the synthetic procedures were also present. The band gap energy values derived from UV-vis spectroscopy are very similar between B-g-C_3N_4, Ni/g-C_3N_4, Co/g-C_3N_4 and Cu/g-C_3N_4, thus suggesting that the deposition of selected metals did not affect their optical properties. Instead, an

increase in the band gap value to 2.96 eV occured in E-g-C_3N_4: this could be due to the quantum confinement effect resulting from exfoliation. The photoelectrochemical activity of g-C_3N_4 samples toward OER was finally tested. All the samples generally show very low performance, with photocurrent density of the order of $\mu A/cm^2$ rather than mA/cm^2, as reported in the literature, and very high resistance. Furthermore, the differences in the values of all the samples are rather small, indicating that exfoliation and doping did not affect the performance as much as expected. This means that the charge transfer is rather slow and electron-hole pair separation is quite poor in the case of the synthesized samples. In particular, in the case of the metal-doped samples it seems that the charge transfer is similar or even lower (like for Ni) than the bulk one. In fact, under light exposure the worst-performing sample is Ni/g-C_3N_4, with a slight increase in this order: Co/g-C_3N_4, Cu/g-C_3N_4, B-g-C_3N_4 and E-g-C_3N_4. The exfoliated sample presents a less disordered structure than the other samples and its band gap was affected by the resulting quantum confinement. This could have led to the presence of a lower number of trap states, more efficient charge transfer, and therefore better performance compared to the other samples. As for the samples containing Ni, Co and Cu, in absence of characterization techniques that could confirm the presence of metals as single atoms, it would be possible to hypothesize a partial agglomeration, leading to the occupation of active sites and reduction of electron mobility.

In the case of NiCo LDH system, the stabilized phases are NiO(OH) and CoO (space groups C12/m1 and F-43m, respectively). NiCo_1:1,26 and NiCo_1.2 showed a very uniform morphology made of nanosheets, which appear to be very thin, while they cannot be identified in the case of Pt/NiCo_1:1.26, Pt/ NiCo_1:2, Ru/NiCo_1:1.26 and Ru/ NiCo_1:2. This change in the morphology could have been caused by the addition of the metal elements, although it is not possible to have evidence of their presence from this kind of analysis. EDS analysis and elemental mapping confirmed the presence not only of Ni and Co, but also of Pt and Ru in the samples with a uniform distribution. However, to verify if such elements are deposited as single atoms, other characterization techniques should be employed, including HAADF-STEM and STM. The structure of LDH samples was confirmed by Raman spectroscopy, even though it cannot give information on single-atom catalysis due to low sensitivity. The electrochemical activity of LDH system toward OER was finally tested. In the case of NiCo_1:1.26 and NiCo_1:2, the phase conversion

to NiO(OH) and CoO from the respective hydroxides may have led to a less ordered structure compared to the stacked structure typical of layered double hydroxides, lowering the performance. However, the values of overpotential of the samples at 10 mA/cm^2 are only slightly higher than those reported by the literature, as mentioned before. Apart from Pt/NiCo_1:1.26, it is generally confirmed that the deposition of metal atoms can improve the performance, with samples with Ru performing better than Pt. Comparing the two molar ratios used, a small difference can be observed between the two samples without metal atoms, while in the case of the other samples, those with molar ratio 1:2 display better performances, having higher current densities, lower Tafel slopes, higher capacities and lower resistances. This suggests that the presence of an increased Co concentration can improve the performance.

For future research, further characterization on the samples of both classes should be performed to investigate whether the deposited metal elements are in form of single atoms. As mentioned, HAADF-STEM and STM could directly image the single atom on the support, giving information on location and spatial distribution. EXAFS and XANES could provide information on the electronic and geometrical structure of the metal species.

Furthermore, it would be interesting to test the photoelectrochemical activity of g-C_3N_4 and electrochemical activity of LDH systems toward HER. For instance, noble metals like Pt are regarded as efficient co-catalysts to enhance the HER performance, so we could verify if the performance of these samples (LDH ones) can be actually improved.

Further experiments, including the investigation of different synthetic routes, could be explored with optimized reaction parameters to improve the morphological, optical and electronic properties, thus leading to an enhanced catalytic performance.

5. Appendix

5.1 X-ray diffraction

X-ray diffraction is a characterization technique which is commonly employed to investigate the structural properties of solid samples. It allows to compute and study many parameters, including the crystalline structure, the size of the microcrystals, the phases present, the dimensions of the unit cell and the type of atoms composing it.

The employed X-rays are electromagnetic waves with wavelengths in the range from 0.5 to 2.5 A, therefore comparable to the interplanar distance of the atoms, which are arranged in an orderly manner in crystalline solids, thus forming the so-called reticular planes. The X-ray beam behaves like a three-dimensional system of coherent sources when it hits a crystalline solid. The interference of the waves emitted by these sources can be observed in the surrounding space. In particular, the beams interfere in a constructive way only if the path difference is an even multiple of the wavelength of the radiation. Naming d the spacing between diffracting planes and θ the incident angle, the difference in path between two beams reflected from two neighbouring planes is $2dsen\theta$. As mentioned, constructive interference occurs only when $n\lambda=2dsen\theta$ where n=2,4,6,… thus obtaining the Bragg equation.

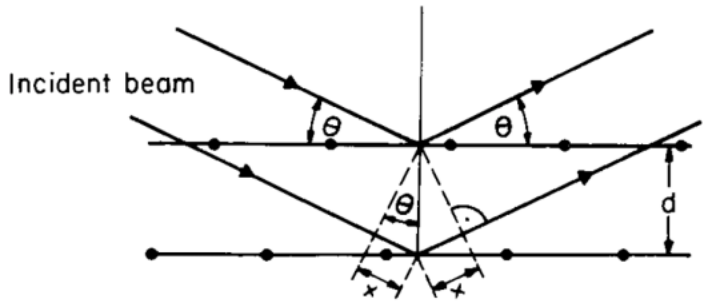

Figure 5.1.1. Schematic of Bragg diffraction.

In particular, samples were analysed as powder. Powder samples present a more random orientation of the crystals. Consequently, when a monochromatic X-ray beam hit them,

they will exhibit the diffraction phenomenon foreseen by Bragg law. The detectors allow to obtain information both on the intensity and on the angle of the diffracted beam. A typical diffraction spectrum reports the intensity of the diffracted ray as a function of the diffraction angle 2θ.

Qualitative analysis of such diffractogram provides various information, including the position of the peaks, which depends exclusively on the unit cell of the material, and the intensity of the peaks, from how many atoms and how they are distributed in the cell. Furthermore, the shape is affected by the sample and instrumental factors.

5.2 Electron scanning microscopy

Electron scanning microscopy is employed to investigate the morphology of the samples. The image provided by the scanning electron microscope (SEM) forms in a cathode ray tube which is synchronized with a beam of charged particles (electrons in this case) scanning the surface of the object.

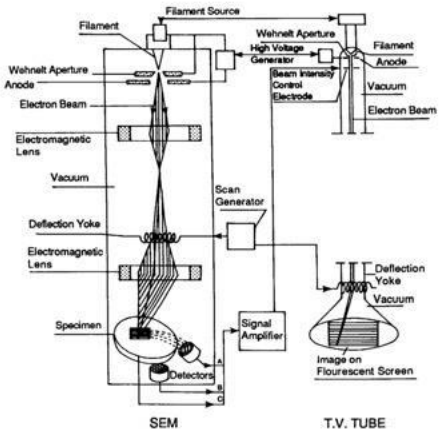

Figure 5.2.1 Schematic representation of an SEM on a television screen.

The electrons are generated by a field emission source, as shown in **figure 5.2.2**: the application of an electric field of adjustable intensity on the single crystal of the source generates a tunnel effect, which eventually leads to the emission of electrons. The electrons are then accelerated by a potential difference varying between 0.3 and 30 kV and applied to the second anode.

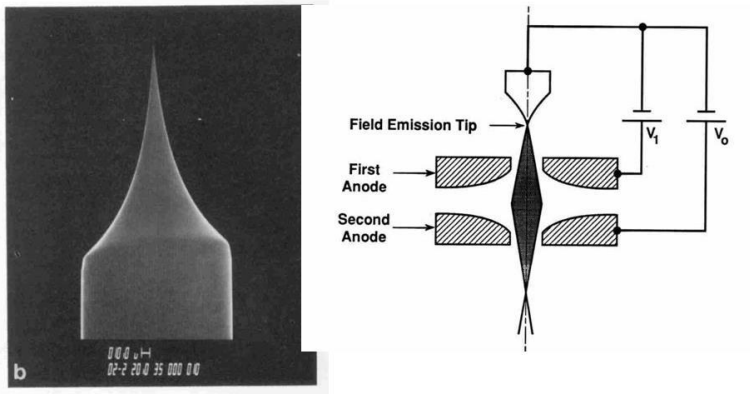

Figure 5.2.2 Representation of a field emission source.

Then, the high-energy electron beam passes through a condensing lens consisting of an electromagnetic lens (**figure 5.2.3**). This is in turn composed by an empty cylinder containing coils where an electric current passes. A magnetic field with the purpose of focusing the incoming electron beam is therefore generated.

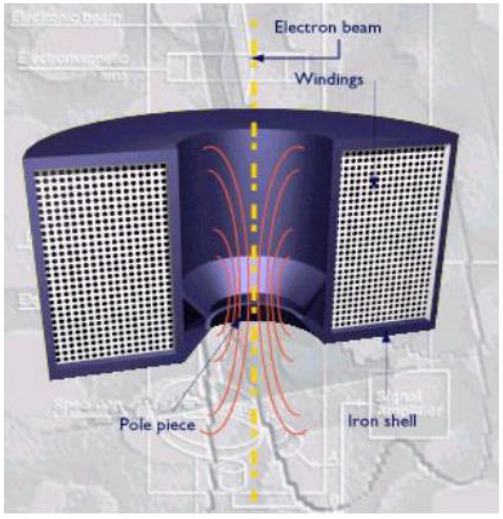

Figure 5.2.3. Schematic of a condensing lens in SEM.

The whole system is kept under high vacuum in order to prevent signal drops due to the loss of electrons from the beam, resulting from the collisions with the molecules present in the air, and to ensure the correct functioning of the source itself. The interaction between primary electrons and sample can be of a different nature and is expressed by the so-called "interaction pear": there are areas of defined volume (interaction volume) in

which the nature of the interaction changes, and therefore the type of signal produced, according the degree of penetration of the electrons, which in turn depends on their energy (**figure 5.2.4**). In the specific case of SEM, the signals of interest are those produced by the secondary and backscattered electrons. The intensity of the signal produced (topographic contrast) is defined as the ratio between the incident electrons and the secondary electrons produced $\delta = \frac{\delta_{se}}{\delta_{in}}$ and it strongly depends on the angle that the incident beam forms with the surface: it increases as the angle increases up to 80 °, and then decrease when approaching 90 °. This may provide information related to the surface topography of our material. Backscattered electrons originate from the elastic scattering of the primary electrons which bounce back after collision with the sample with an energy close to the original and therefore come from a deeper area of the interaction pear. The scattering efficiency $\eta = \frac{\eta_{BS}}{\eta_{in}}$ strongly depends on the atomic number Z since the greater the size of the nucleus, the greater the number of incident electrons that are pushed back when hitting the nucleus.

The detection of secondary electrons allows to observe the sample at high resolution, both at high and low magnifications. The depth of field is very large, thus allowing to focus irregular rough surfaces.

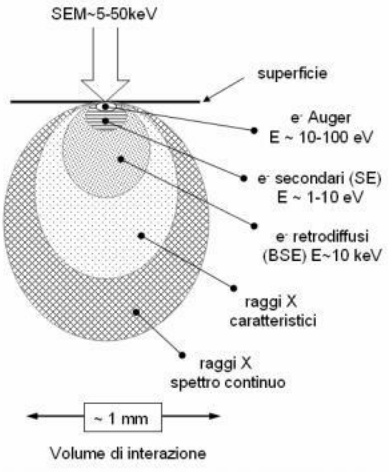

Figure 5.2.4. Schematic of the interaction pear formed by the interaction between primary electrons and sample.

5.3. EDS

The system is composed of a SEM equipped with EDX, which is a particular type of detector that exploits the interaction between X-rays and the material. The detector may be constituted by a single silicon crystal doped with lithium, coated with a conductive layer of gold at the extremes and maintained at a temperature of 77K with liquid nitrogen or by a high purity germanium crystal. The operating principle exploits the production of electric current generated by the interaction between photons and the crystal and then amplified. It is a non-destructive technique that is mainly used for the qualitative and elemental analysis of solid samples which are electrical conductors and exhibit stability under low pressure conditions and electron bombardment.

5.4 UV-vis spectroscopy

UV-vis spectroscopy is a qualitative and quantitative technique which allows to measure how much a chemical substance absorbs light. This is possible by measuring the intensity of the light passing through the sample compared to the one passing through a blank or a reference sample. Spectroscopically, what is observed is the absorbance of the electromagnetic radiation that excite the electrons from the ground state to the first singlet excited state of the material. In the electromagnetic spectrum the UV-vis region covers a range from 1.5 to 6.2 eV corresponding to wavelengths from 800 to 200 nm. Using a spectrophotometer and according to the type of measurement (absorption, transmission or reflection), it is possible to determine the concentration of a known chemical substance by measuring the number of photons (therefore the light intensity) reaching the detector. This type of measure is based on the Lambert Beer law:

$$A = \log\left(\frac{I_0}{I}\right) = \varepsilon bc$$

Where A is the absorbance of the sample, I_0 is the intensity of the incident light, I the intensity of the transmitted light through the sample, ε is the extinction coefficient (or

molar absorptivity), b is the path length through the sample and c the concentration of the absorbing species.

The instrument employed in this kind of analysis is a spectrophotometer, which measures and compares the transmitted and incident light intensities, thus determining the transmittance (usually expressed as percentage %T). From that the absorbance is calculated using the equation $A = -log\frac{\%T}{100\%}$. It is possible to also measure reflectance by specifically configuring the instrument. In this case, the intensity of the reflected light by the sample is measured and compared to the one reflected by a reference. The ratio between them is the reflectance, usually expressed as %R.

In this last case, the technique is also known as diffuse reflectance UV-vis spectroscopy. It is mainly employed to analyse samples in powder form with minimal sample preparation. This kind of analysis takes advantage of a so called integrating sphere. The sample is placed in front of the incident light window and the light reflected is concentrated on the detector using the sphere. When light hit the sample with an angle of 0°, specular light exits the integrating sphere and is not detected, thus only diffuse reflected light is measured. Reflectance can be related to the absorbance by means of the Kubelka-Munk theory. The absolute remittance (R_∞) is calculated as the ratio of the light reflected by the sample (J) and the light incident on the sample: $R_\infty = \frac{J}{I_0}$, where indicates that the sample is infinitely thick. However, since it is not practical, the relative remittance ($R_\infty{}'$) is computed as $R_\infty{}' = \frac{R_{\infty\,sample}}{R_{\infty\,standard}}$. From the Kubelka-Munk theory the following function is derived: $F(R) = \frac{(1-R_\infty)^2}{2R_\infty}$, which relate to the absorbance of the sample.

This value can then be used for the calculation of the band gap energy E_g of the sample. E_g can be determined as the intersection of the linear part of the so called Tauc plot with the x-axis. This kind of graph is obtained by plotting the energy (eV) against F(R)hν, according to the equation: $\alpha = A(h\nu - E_g)^n/h\nu$, where α, h, ν, A and E_g are the absorption coefficient, Plank's constant, light frequency, constant and band gap energy, respectively. The value for n depends on the optical transition of the semiconductor (n = 1/2 for direct semiconductors and n = 2 for indirect ones).

5.5 Raman spectroscopy

Raman spectroscopy is a characterization technique which is very useful in the identification of chemical species. This is possible thanks to the detection of particular interactions of the sample with radiation. In particular, it exploits Stokes and Anti-Stokes scattering (**figure 5.5.1**) by observing the change in the energy between incident and scattered photons associated with such transitions.

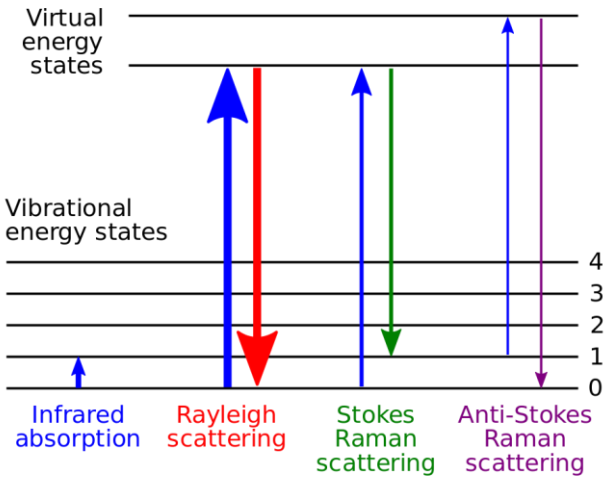

Figure 5.5.1. Schematic of the possible scatterings by a molecule excited by photons.

This change is usually measured as the change in wavenumber compared to the incident light source (Raman shift $\Delta\tilde{\nu}$). Measurements could be taken at any wavelength since the shift is measured in wavenumber, but near infrared or visible light sources are usually employed.

Raman activity is mainly affected by the polarizability of a bond, that is a measure of how much it can be deformed in an electric field. Therefore, this depends on how easy the displacement of the electrons from the bond, thus the formation of a temporary dipole, is. For instance, an intense Raman signal will occur when the polarizability is large due to a high concentration of loosely held electrons in a bond. This leads to a better sensitivity to

the molecular framework compared to specific functional groups, like in the case of IR spectroscopy.

In light of this, the information provided by this technique is related to the metal ligand bond, allowing then to study the structure, composition and stability of the sample. This appear particularly useful in the case of those compounds with low absorption frequencies in the IR.

6. Bibliography

[1] F. Yang, P. Song, W. Xu. The Applications of 2D Nanomaterials in Energy-Related Process. *Adapting 2D Nanomater for Advanced Applications*. Chapter 10. J. *Am. Chem. Soc.* 219-251 (2020).

[2] H. Jin, C. Guo, X. Liu, A. Vasileff, Y. Jiao, Y. Zheng, S. Qiao. Emerging Two-Dimensional Nanomaterials for Electrocatalysis. *Chem Rev*. **118**, 6337-6408 (2018).

[3] T. Hu, T. Mei, Y. Wang, X. Weng, R. Liang, M. Wei. Two-dimensional nanomaterials: fascinating materials in biomedical field. *Sci. Bull.* **64**, 1707–1727 (2019).

[4] F. Fina, S.K. Callear, G.M. Carins, J.T.S. Irvine. Structural investigation of graphitic carbon nitride via XRD and neutron diffraction. *Chem. Mater.* **27**, 2612–2618 (2015).

[5] A. Wang, C. Wang, L. Fu, W.W. Yucheng. Recent Advances of Graphitic Carbon Nitride-Based Structures and Applications in Catalyst, Sensing, Imaging, and LEDs. *Nano-Micro Lett.* **9**, 47 (2017).

[6] A. Thomas, A. Fisher, F. Goettmann, M. Antonietti, J.O. Müller, R. Schlögl, J.M. Carlsson. Graphitic carbon nitride materials: Variation of structure and morphology and their use as metal-free catalysts. *J. Mater. Chem.* **18**, 4893–4908 (2008).

[7] J. Hong, X. Xia, Y. Wang, R. Xu. Mesoporous carbon nitride with *in situ* sulfur doping for enhanced photocatalytic hydrogen evolution from water under visible light. *J. Mater. Chem*. **22**, 15006–15012 (2012).

[8] X. Wang, K. Maeda, X. Chen, K. Takanabe, K. Domen, Y. Hou, X. Fu, M. Antonietti. Polymer Semiconductors for Artificial Photosynthesis: Hydrogen Evolution by Mesoporous Graphitic Carbon Nitride with Visible Light. *J. Am. Chem. Soc*. **131**, 5, 1680–1681 (2009).

[9] S. Zhang, H. Dong, C. An, Z. Li, D. Xu, K. Xu, Z. Wu, J. Shen, X. Chen, S. Zhang. One-pot synthesis of array-like sulfur-doped carbon nitride with covalently crosslinked ultrathin MoS_2 cocatalyst for drastically enhanced photocatalytic hydrogen evolution. *J. Mater. Sci. Technol.* **75**, 59–67 (2021).

[10] M. Ismael, Y. Wu, D.H. Taffa, P. Bottke, M. Wark. Graphitic carbon nitride synthesized by simple pyrolysis: Role of precursor in photocatalytic hydrogen production. *New J. Chem.* **43**, 6909–6920 (2019).

[11] Y. Zhang, J. Liu, G. Wu, W. Chen. Porous graphitic carbon nitride synthesized via direct polymerization of urea for efficient sunlight-driven photocatalytic hydrogen production. *Nanoscale*. **4**, 5300-5303 (2012).

[12] G. Zhang, J. Zhang, M. Zhang, X. Wang. Polycondensation of thiourea into carbon nitride semiconductors as visible light photocatalysts. *J. Mater. Chem.* **22**, 8083–8091 (2012).

[13] F. Dong, Y. Sun, L. Wu, M. Fu, Z. Wu. Facile transformation of low cost thiourea into nitrogen-rich graphitic carbon nitride nanocatalyst with high visible light photocatalytic performance. *Catal. Sci. Technol.* **2**, 1332–1335 (2012).

[14] C. Prasad, H. Tang, I. Bahadur. Graphitic carbon nitride based ternary nanocomposites: From synthesis to their applications in photocatalysis: A recent review. *J. Mol. Liq.* **281**, 634–654 (2019).

[15] S. P. Pattnaik, A. Behera, S. Martha, R. Acharya, K. Parida. Facile synthesis of exfoliated graphitic carbon nitride for photocatalytic degradation of ciprofloxacin under solar irradiation. *J. Mater. Sci.* **54**, 5726–5742 (2019).

[16] P. Niu, L. Zhang, G. Liu, H.M. Cheng. Graphene-like carbon nitride nanosheets for improved photocatalytic activities. *Adv. Funct. Mater.* **22**, 4763–4770 (2012).

[17] C. Hu, F. Chen, Y. Wang, N. Tian, T. Ma, Y. Ma, Y. Zhang, H. Huang. Exceptional Cocatalyst-Free Photo-Enhanced Piezocatalytic Hydrogen Evolution of Carbon Nitride Nanosheets from Strong In-Plane Polarization. *Adv. Mater***.** 1–9 (2021).

[18] J. Zhang, Y. Chen, X. Wang. Two-dimensional covalent carbon nitride nanosheets: synthesis, functionalization, and applications. *Energy Environ. Sci*. **8**, 3092–3108 (2015).

[19] S. Yang, Y. Gong, J. Zhang, L. Zhan, L. Ma, Z. Fang, R. Vajtai, X. Wang, P.M. Ajayan. Exfoliated graphitic carbon nitride nanosheets as efficient catalysts for hydrogen evolution under visible light. *Adv. Mater.* **25**, 2452–2456 (2013).

[20] Q. Lin, L. Li, S. Liang, M. Liu, J. Bi, L. Wu. Efficient synthesis of monolayer carbon nitride 2D nanosheet with tunable concentration and enhanced visible-light photocatalytic activities. *Appl. Catal. B Environ.* **163**, 135–142 (2015).

[21] G. Mishra, B. Dash, S. Pandey, S. Layered double hydroxides: A brief review from fundamentals to application as evolving biomaterials. *Appl. Clay Sci.* **153**, 172–186 (2018).

[22] D.G. Evans, X. Duan. Preparation of layered double hydroxides and their applications as additives in polymers, as precursors to magnetic materials and in biology and medicine. *Chem. Commun*. 485–496 (2006).

[23] C. Li, M. Wei, D.G. Evans, X. Duan. Layered Double Hydroxide-based Nanomaterials as Highly Efficient Catalysts and Adsorbents. *Small*. **10**, 4469–4486 (2014).

[24] Li, P. M. Wang, X. Duan, L. Zheng, X. Cheng, Y. Zhang, Y. Li, Q. Ma, Z. Feng, W. Liu, X. Sun. Boosting oxygen evolution of single-atomic ruthenium through electronic coupling with cobalt- iron layered double hydroxides. *Nat. Commun.* **10**, 1–11 (2019).

[25] G. Fan, F. Li, D.G. Evans, X. Duan. Catalytic applications of layered double hydroxides: recent advances and perspectives. *Chem Soc Rev*. **43**, 7040–7066 (2014).

[26] X. Li, D. Du, Y. Zhang, W. Xing, Q. Xue, Z. Yan. Layered double hydroxides toward high- performance supercapacitors. *J. Mater. Chem*. **5**, 15460–15485 (2017).

[27] X. Lu, H. Xue, H. Gong, M. Bai, D. Tang, R. Ma, T. Sasaki. 2D Layered Double Hydroxide Nanosheets and Their Derivatives Toward Efficient Oxygen Evolution Reaction. *Nano-Micro Lett.* **12**, 12-86 (2020).

[28] P. Zhou, J. He, Y. Zou, Y. Wang, C. Xie, R. Chen, S. Zang, S. Wang. Single-crystalline layered double hydroxides with rich defects and hierarchical structure by mild reduction for enhancing the oxygen evolution reaction. *Sci. China Chem.* **62**, 1365–1370 (2019).

[29] F. Song, X. Hu. Exfoliation of layered double hydroxides for enhanced oxygen evolution catalysis. *Nat. Commun.* **5**, 4477 (2014).

[30] B. Zhang, T. Fan, N. Xie, G. Nie, H. Zhang. Versatile Applications of Metal Single-Atom @ 2D Material Nanoplatforms. *Adv. Sci.* **6**, (2019).

[31] S. Mitchell, J. Pérez-Ramírez. Single atom catalysis: a decade of stunning progress and the promise for a bright future. *Nat. Commun.* **11**, 4302, 10–12 (2020).

[32] X. Yang, A. Wang, B. Qiao, J. Liu, T. Zhang. Single-Atom Catalysts: A New Frontier in Heterogeneous Catalysis. **46**, 8, 1740-1748 (2013).

[33] R. Gusmão, M. Veselý, Z. Sofer. Recent Developments on the Single Atom Supported at 2D Materials beyond Graphene as Catalysts. *ACS Catal.* **10**, 9634–9648 (2020).

[34] J. Wu, L. Xiong, B. Zhao, M. Liu, L. Huang. Densely Populated Single Atom Catalysts. *Small Methods*. **1900540**, 4, 1–16 (2020).

[35] J. Liu. Single-atom catalysis for a sustainable and greener future. *Curr. Opin. Green.* **22**, 54-64 (2020).

[36] A. Wang, J. Li, T. Zhang. Heterogeneous single-atom catalysis. *Nat. Rev. Chem.* **2**, 65-81 (2018).

[37] J. Fu, S. Wang, Z. Wang, K. Liu, H. Li, H. Liu, J. Hu, X. Xu, H. Li, M. Liu. Graphitic carbon nitride based single-atom photocatalysts. *Front. Phys.* **15**, 28–30 (2020).

[38] Y. Li, J. Li, W. Yang, X. Wang. Implementation of ferroelectric materials in photocatalytic and photoelectrochemical water splitting. *Nanoscale Horizons.* **5**, 1174-1187 (2020).

[39] I. Roger, M. A. Shipman, M. D. Symes. Earth-abundant catalysts for electrochemical and photoelectrochemical water splitting. *Nat. Rev. Chem.* **1**, (2017).

[40] Y. Shi, B. Zhang. Recent advances in transition metal phosphide nanomaterials: synthesis and applications in hydrogen evolution reaction. *Chem. Soc. Rev.* **45**, 1529-1541 (2016).

[41] S. Arumugam, Y. Toku, Y. Ju. Fabrication of γ-Fe_2O_3 nanowires from Abundant and Low-cost Fe Plate for Highly Effective electrocatalytic Water Splitting. *Sci. Rep.* **10**, 1-11 (2020).

[42] X. Li, X. Hao, A. Abudula, G. Guan. Nanostructured catalysts for electrochemical water splitting: current state and prospects. *J. Mater. Chem. A.* **4**, 11973-12000 (2916).

[43] Z. Chen, X. Liu, P. Xin, H. Wang, Y. Wu, C. Gao, Q. He, Y. Jiang, Z. Hu, S. Huang. Interface engineering of NiS@MoS_2 core-shell microspheres as an efficient catalyst for hydrogen evolution reaction in both acidic and alkaline medium. *J. Alloy Compd.* **853** (2021).

[44] L. Li, P. Wang, Q. Shao, X. Huang. Metallic nanostructures with low dimensionality for electrochemical water splitting. *Chem. Soc. Rev.* **49**, 3072-3106 (2020).

[45] S. Anantharaj, S. Noda. Amorphous Catalysts and Electrochemical Water Splitting: An Untold Story of Harmony. *Small.* **16** (2020).

[46] J. Wang, X. Yue, Y. Yang, S. Sirisomboonchai, P. Wang, X. Ma, A. Abudula, G. Guan. Earth-abundant transition-metal-based bifunctional catalysts for overall electrochemical water splitting: A review. *J. Alloys Compd.* **819** (2020).

[47] K. C. Majhi, M. Yadav. Bimetallic chalcogenide nanocrystallites for efficient electrocatalysts for overall water splitting. *J. Alloys Compd.* **852** (2021).

[48] V. Vij, S. Sultan, A. M. Harzandi, A. Meena, J. N. Tiwari, W. G. Lee, T. Yoon, K. S. Kim. Nickel-Based Electrocatalysts for Energy-Related Applications: Oxygen Reduction, Oxygen Evolution, and Hydrogen Evolution Reactions. *ACS Catal.* **7**, 7196-7225 (2017).

[49] J. Wang, W. Cui, Q. Liu, Z. Xing, A. M. Asiri, X. Sun. Recent Progress in Cobalt-Based Heterogeneous Catalysts for Electrochemical Water Splitting. *Adv. Mater.* **28**, 215-230 (2016).

[50] U. Aftab, A. Tahira, A. Gradone, V. Morandi, M.I. Abro, M. M. Baloch, A. Liaquat Bhatti, A. Nafady, A. Vomiero Z.H. Ibupoto. Two step synthesis of TiO_2-Co_3O_4 composite for efficient oxygen evolution reaction. *Int. J. Hydrogen Energy.* **46**, 9110-9122 (2021).

[51] A. Fujishima, K. Honda. Electrochemical Photolysis of Water at a Semiconductor Electrode. *Nature*. **238**, 37-38 (1972).

[52] A. Govind Rajan, J. M. P. Martirez, E. A. Carter. Why Do We Use the Materials and Operative Conditions We Use for Heterogeneous (Photo)Electrochemical Water Splitting? *ACS Catal.* **10**, 11177-11234 (2020).

[53] C. Ros, T. Andreu, J. R. Morante. Photoelectrochemical water splitting: a road from stable metal oxides to protected thin film solar cells. *J. Mater. Chem. A.* **8**, 10625-10669 (202).

[54] C. Li, J. He, Y. Xiao, Y. Li, J. J. Delaunay. Eart-abundant Cu-based metal oxide photocathodes for photoelectrochemical water splitting. *Energy Environ. Sci.* **13**, 3269-3306 (2020).

[55] Z. Haider, H. W. Yim, H. W. Lee, H. Kim. Surface and bulk modification for advanced electrode design in photoelectrochemical water splitting. *Int. J. Hydrogen Energy*. **45**, 5793-5815 (2020).

[56] S. K. Saraswat, D. D. Rodene, R. B. Gupta. Recent Advancements in semiconductor materials for photoelectrochemical water splitting for hydrogen production using visible light. *Renew. Sustain. Energy Rev.* **89**, 228-248 (2018).

[57] L. Mascaretti, A. Dutta, Š. Kment, V. M. Shalaev, A. Boltasseva, R. Zbořil, A. Naldoni. Plasmon-Enhanced Photoelectrochemical Water Splitting for Efficient Renewable Energy Storage. *Adv. Mater.* **31**, (2019).

[58] Z. Wang, C. Li, K. Domen. Recent developments in heterogeneous photocatalysts for solar-driven overall water splitting. *Chem. Soc. Rev.* **48**, 2019-2125 (2019).

[59] P. Dias, T. Lopes, L. Meda, L. Andrade, A. Mendes. Photoelectrochemical water splitting using WO_3 photoanodes: The substrate and the temperature roles. *Phys. Chem. Chem. Phys.* **18**, 5232-5243 (2016).

[60] C. V. Reddy, K. R. Reddy, N. P. Shetti, J. Shim, T. M. Aminabhavi, D. D. Dionysiou. Metal-organic frameworks (MOFs)-based efficient heterogeneous photocatalysts: Synthesis, properties and its applications in photocatalytic hydrogen generation, CO_2 reduction and photodegradation of organic dyes. *Int. J. Hydrogen Energy*. **45**, 7656-7679 (2020).

[61] Z. Chen, S. Mitchell, E. Vorobyeva, R.K. Leary, R. Hauert, T. Furnival, Q. M. Ramasse, J.M. Thomas, P.A. Midgley, D. Dontsova, M. Antonietti, S. Pogodin, N. Lopez, J. Pérez-Ramìrez. Stabilization of Single Metal Atoms on Graphitic Carbon Nitride. *Adv. Funct. Mater*. **27** (2017).

[62] G. Vilé, D. Albani, M. Nachtegaal, Z. Chen, D. Dontsova, M. Antonietti, N. Lopez, J. Pérez-Ramìrez. A Stable Single-Site Palladium Catalyst for Hydrogenations. *Angew. Chem. Int. Ed*. **54**, 11265–11269 (2015).

[63] R. Li, Z. Hu, X. Shao, P. Cheng, S. Li, W. Yu, W. Lin, D. Yuan. Large scale synthesis of NiCo layered double hydroxides for superior asymmetric electrochemical capacitor. *Sci. Rep.* **6**, 1–9 (2016).

[64]. L. Cheng, H. Yin, C. Cai, J. Fan, Q. Xiang. Single Ni Atoms Anchored on Porous Few-Layer g-C 3 N 4 for Photocatalytic CO 2 Reduction: The Role of Edge Confinement. *Small*. **16**, 1–10 (2020).

[65] M.D. Capobianco, B. Pattengale, J. Neu, C. A. Schmuttenmaer. Single Copper Atoms Enhance Photoconductivity in g-C_3N_4. *J. Phys. Chem. Lett.* **11**, 8873−8879 (2020).

[66] Q. Ruan, M.K. Bayazit, V. Kiran, J. Xie, Y. Wang, J. Tang. Key factors affecting photoelectrochemical performance of g-C3N4 polymer films. *Chem. Commun.* **55**, 7191–7194 (2019).

[67] J. Oh, H. Ryu, W.J. Lee. Effects of Fe doping on the photoelectrochemical properties of CuO photoelectrodes. *Compos. Part B Eng.* **163**, 59–66 (2019).

[68] K. Qin, L. Wang, S. Wen, L. Diao, P. Liu, J. Li, L. Ma, C. Shi, C. Zhong, W. Hu, E. Liu, N. Zhao. Designed synthesis of NiCo-LDH and derived sulfide on heteroatom-doped edge-enriched 3D rivet graphene films for high-performance asymmetric supercapacitor and efficient OER. *J. Mater. Chem. A.* **6**, 8109–8119 (2018).

[69] R. Fan, Q. Mu, Z. Wei, Y. Peng, M. Shen. Atomic Ir-doped NiCo layered double hydroxide as a bifunctional electrocatalyst for highly efficient and durable water splitting. *J. Mater. Chem. A.* **8**, 9871–9881 (2020).

[70]. J. Wei, S. Qin, J. Yang, H. Ya, W. Huang, H. Zhang, B. J. Hwang, Z. Tian, J.F. Li. Probing Single-Atom Catalysts and Catalytic Reaction Processes by Shell-Isolated Nanoparticle-Enhanced Raman Spectroscopy. *Angew. Chem. Int. Ed.* **60**, 9306–9310 (2021).